

# Tracing Chemical Depletion in Evolved Binaries Hosting Second-Generation Transition Discs

Maksym Mohorian,<sup>1,2\*</sup> Devika Kamath,<sup>1,2,3</sup> Meghna Menon,<sup>1,2</sup> Anish M. Amarsi,<sup>4</sup>

Hans Van Winckel,<sup>5</sup> Claudia Fava,<sup>1,2</sup> and Kateryna Andrych<sup>1,2</sup>

<sup>1</sup>*School of Mathematical and Physical Sciences, Macquarie University, Balaclava Road, Sydney, NSW 2109, Australia*

<sup>2</sup>*Astrophysics and Space Technologies Research Centre, Macquarie University, Balaclava Road, Sydney, NSW 2109, Australia*

<sup>3</sup>*INAF, Osservatorio Astronomico di Roma, Via Frascati 33, I-00077 Monte Porzio Catone, Italy*

<sup>4</sup>*Theoretical Astrophysics, Department of Physics and Astronomy, Uppsala University, Box 516, SE-751 20 Uppsala, Sweden*

<sup>5</sup>*Institute of Astronomy, KU Leuven, Celestijnenlaan 200D, 3001 Leuven, Belgium*

Accepted XXX. Received YYY; in original form ZZZ

## ABSTRACT

The mechanisms responsible for chemical depletion across diverse astrophysical environments are not yet fully understood. In this paper, we investigate chemical depletion in post-AGB/post-RGB binary stars hosting second-generation transition discs using high-resolution optical spectra from HERMES/Mercator and UVES/VLT. We performed a detailed chemical abundance analysis of 6 post-AGB/post-RGB stars and 6 post-AGB/post-RGB candidates with transition discs in the Galaxy and in the Large Magellanic Cloud. The atmospheric parameters and elemental abundances were obtained through 1D LTE analysis of chemical elements from C to Eu, and 1D NLTE corrections were incorporated for elements from C to Fe. Our results confirmed that depletion efficiency, traced by the [S/Ti] abundance ratio, is higher in post-AGB/post-RGB binaries with transition discs compared to the overall sample of post-AGB/post-RGB binaries. We also examined correlations between derived abundances and binary system parameters (astrometric, photometric, orbital, pulsational). Additionally, we compared the depletion patterns in our sample to those observed in young stars with transition discs and in the interstellar medium. We confirmed that the depletion is significantly stronger in post-AGB/post-RGB binaries with transition discs than in young stars with transition discs. Furthermore, we found that [X/Zn] abundance ratio trends of volatile and refractory elements in post-AGB/post-RGB binaries with transition discs generally resemble similar trends in the interstellar medium (except for trends of [Si/Zn] and [Mg/Zn] ratios). These findings, although based on a limited sample, provide indirect constraints for depletion mechanism in circumbinary discs around post-AGB/post-RGB stars.

**Key words:** *stars: evolution, stars: binaries, stars: AGB and post-AGB, stars: chemically peculiar, stars: abundances, techniques: spectroscopic*

## 1 INTRODUCTION

One of the most complex aspects of binary star evolution is the interaction between binaries and circumbinary discs (Heath & Nixon 2020; Penzlin et al. 2022; Coleman et al. 2022; Zagarria et al. 2023). These discs, characterised by intricate dynamics and varying dust content, significantly influence observable properties of the host binary, such as infrared excess (Itoh et al. 2015), accretion rates (Izzard & Jermyn 2023), orbital eccentricity (Heath & Nixon 2020), and jet activity (Bollen et al. 2022). The diversity of dust content in circumbinary discs results from dust condensation being dependent on the chemical composition of the condensing mixture and the physical conditions of the environment, such as pressure and temperature (Lodders 2003; Wood et al. 2019). While the

process of dust condensation is well-studied for protoplanetary discs around young single stars (Lagage & Pantin 1994; Birnstiel et al. 2016), the effect of binarity on dust condensation in circumbinary discs around evolved binary stars remains poorly explored (Oomen et al. 2020; González-Bolívar et al. 2024).

During the evolution along the asymptotic giant branch (AGB) or red giant branch (RGB), low- and intermediate-mass stars ( $M \sim 0.8 - 8M_{\odot}$ ) in a binary system can fill their Roche lobe, leading to mass loss that terminates AGB/RGB evolution. The primary star then transitions to the post-asymptotic giant branch (post-AGB) or post-red giant branch (post-RGB) stage (van Winckel 2003; Kamath et al. 2016; Van Winckel 2018; Kluska et al. 2022). While the binary interactions between the post-AGB/post-RGB primary star and the secondary component (often a main sequence star; Oomen et al. 2018) remain poorly understood, observational studies reveal that these interactions often re-

\* E-mail: maksym.mohorian@students.mq.edu.au

sult in the formation of a stable disc of circumstellar gas and dust (with radii  $< 1000$  AU; de Ruyter et al. 2006; Deroo, P. et al. 2006; Bujarrabal et al. 2015; Hillen, M. et al. 2016; Bujarrabal et al. 2018; Kluska et al. 2022; Corporaal et al. 2023; Gallardo Cava 2023).

The presence of the disc around post-AGB binaries was observationally established by the distinct pattern in spectral energy distribution (SED; de Ruyter et al. 2005, 2006; Kamath et al. 2014; Gezer et al. 2015; Kamath et al. 2015; Kluska et al. 2022). This pattern includes a near-infrared (near-IR) dust excess, indicative of hot dust in the system (van Winckel 2003; Oomen et al. 2018). Interferometric imaging studies resolved the inner rim of circumbinary discs in several post-AGB/post-RGB binary systems, which in many cases is close to the dust sublimation radius (typically,  $\sim 5$ – $30$  AU; Kluska et al. 2019; Corporaal et al. 2023). In addition, high-resolution polarimetric imaging studies with SPHERE revealed complex substructures in circumbinary discs around post-AGB/post-RGB stars, including rings, spirals, and arc-like features (Ertel et al. 2019; Andrych et al. 2023). Moreover, the outer regions of these discs are known to display crystallisation (Gielen et al. 2011; Hillen et al. 2015) and grain growth (Sciicluna et al. 2020). Additionally, circumbinary discs around post-AGB/post-RGB binaries display Keplerian rotation based on position–velocity maps of  $^{12}\text{CO}$  (Bujarrabal et al. 2015; Gallardo Cava et al. 2023).

Recently, Kluska et al. (2022) compiled a comprehensive sample of 85 Galactic post-AGB binaries and their low-luminosity analogues, dusty post-RGB stars. Using the near-IR and mid-IR colours (2MASS  $H - K$  and WISE  $W_1 - W_3$ , respectively), Kluska et al. (2022) categorised the discs around Galactic post-AGB/post-RGB binaries in three groups: i) full discs, where the dust in the disc extends from the dust sublimation radius outward, ii) transition discs, where IR colours suggest the presence of large dust cavities in the inner discs, and iii) discs with significant lack of IR excess, which points to virtual absence of circumbinary dust (we refer to these discs as dust-poor, though this group includes gas-poor debris discs). A subsequent mid-IR interferometric study of full and transition disc candidates in the Galaxy by Corporaal et al. (2023) confirmed the presence of this gap (the dust inner rims in transition disc systems are 2.5–7.5 times larger than the corresponding dust sublimation radii). This subset of transition disc targets is the centrepiece of this study (see Section 2).

The interaction between the binary star and the circumbinary disc significantly affects the surface composition of the post-AGB/post-RGB star. In particular, the post-AGB/post-RGB binaries with circumbinary discs exhibit photospheric chemical depletion (hereafter referred to as depletion) with a notable underabundance of refractory elements (i.e. those with condensation temperatures  $T_{\text{cond}} > 1250$  K, such as Al, Fe, Ti, and the majority of the slow neutron capture process elements) relative to volatile elements (i.e. those with condensation temperatures  $T_{\text{cond}} < 1250$  K, like S, Zn, Na, and K; Gielen et al. 2009; Gezer et al. 2015; Kamath & Van Winckel 2019). The exact mechanism behind chemical depletion in post-AGB/post-RGB stars is not yet fully understood. However, it is believed to result from the chemical fractionation of gas and dust in the circumbinary disc and subsequent accretion of a small portion of this pure gas onto the photosphere of the primary component (Waters et al. 1992; Oomen et al.

2020). The efficiency of the gas-dust fractionation is specific to each chemical element and depends on its condensation temperature,  $T_{\text{cond}}$  (Lodders 2003; Wood et al. 2019). Consequently, mostly refractory dust particles are settling in the mid-plane of the disc, while mostly volatile gas is partially re-accreted onto the binary (Mösta et al. 2019; Muñoz et al. 2019).

Observational studies of depletion in post-AGB/post-RGB binaries in the Galaxy and the Magellanic Clouds (Giridhar et al. 1998; Maas et al. 2002; de Ruyter et al. 2005; Giridhar et al. 2005; de Ruyter et al. 2006; Maas et al. 2007; Van Winckel et al. 2012; Rao & Giridhar 2014; De Smedt et al. 2012, 2014, 2015, 2016) showed that the relative abundances  $[\text{X}/\text{H}]^1$  are prominently decreased for those elements, which have high condensation temperatures  $T_{\text{cond}}$ . This leads to a prominent break in the plots of condensation temperature  $T_{\text{cond}}$  vs. relative abundance  $[\text{X}/\text{H}]$  for post-AGB/post-RGB binaries (Oomen et al. 2019). The condensation temperature at the break – the turn-off temperature  $T_{\text{turn-off}}$  – has a wide range of values within the Galactic subsample (from 800 to 1500 K; Kluska et al. 2022).

The rate (or efficiency) of the chemical depletion in post-AGB/post-RGB binary stars is traced by a volatile-to-refractory abundance ratio, usually  $[\text{Zn}/\text{Ti}]$  ratio (Gezer et al. 2015; Oomen et al. 2019). Depletion efficiency may be categorised into the following groups: mild ( $[\text{Zn}/\text{Ti}] < 0.5$  dex), moderate ( $0.5 \text{ dex} < [\text{Zn}/\text{Ti}] < 1.5$  dex), or strong ( $[\text{Zn}/\text{Ti}] > 1.5$  dex). Kluska et al. (2022) showed that the observed depletion efficiency ( $[\text{Zn}/\text{Ti}]$  ratio) is generally the highest in the subsample of transition disc candidates. Additionally, the high-temperature end of depletion profile in the  $T_{\text{cond}}$ - $[\text{X}/\text{H}]$  plots (i.e. for elements with  $T_{\text{cond}} > T_{\text{turn-off}}$ ) may follow a linear trend (“saturated” profile) or a two-piece linear fit with a horizontal plateau at higher condensation temperatures (“plateau” profile; Waelkens et al. 1991; Oomen et al. 2019, 2020). Theoretical studies using the detailed MESA stellar evolution models confirmed that the observed depletion profiles in post-AGB binaries (including the breaks at  $T_{\text{turn-off}}$  and “plateau” start) may be qualitatively reproduced by dilution of re-accreted metal-poor gas from the disc with the pristine composition of the stellar surface (Oomen et al. 2019, 2020).

C, N, and O (CNO elements) are generally excluded from the depletion profiles, because it is difficult to separate their depletion from the effects of nucleosynthetic and mixing processes that occur during AGB/RGB phase (Mohorian et al. 2024; Menon et al. 2024). Current stellar evolution models predict that surface abundances of C and N are significantly modified by mixing processes on AGB/RGB, while surface abundance of O is unaffected by mixing processes in low-mass ( $M < 2M_{\odot}$ ) AGB stars and in RGB stars (Ventura et al. 2008; Karakas & Lattanzio 2014; Ventura et al. 2020; Kobayashi et al. 2020; Kamath et al. 2023). This highlights the complexity of disentangling chemical impacts on CNO abundances from evolution and re-accretion.

In this study, we further explore the disc-binary interaction by systematically investigating chemical depletion in post-

<sup>1</sup>  $[\text{X}/\text{H}] = \log \frac{N(\text{X})}{N(\text{H})} - \log \frac{N(\text{X})_{\odot}}{N(\text{H})_{\odot}} + 12$ , where  $N(\text{X})$  and  $N(\text{H})$  are the number abundances of element X and hydrogen, respectively. Symbol  $\odot$  denotes the corresponding solar abundances.

AGB/post-RGB binary stars. Our focus is on the subset of post-AGB/post-RGB binaries hosting second-generation transition discs, as these systems share key similarities with young stellar objects (YSOs) that host planet-forming discs. The goals of this study are: i) to homogeneously derive the depletion profiles of transition disc targets, ii) to examine the connection between depletion and other observational parameters, and iii) to establish a comparative study between depletion patterns observed in post-AGB/post-RGB binary stars, YSOs, and the interstellar medium (ISM). To achieve our goals, we derived precise atmospheric parameters and elemental abundances using 1D local thermodynamic equilibrium (LTE) models for chemical elements from C to Eu. In addition, we accounted for 1D non-LTE (NLTE) effects for a representative set of chemical elements (C, N,  $\alpha$ -elements, and Fe). In Section 2, we provide an overview of our target sample. In Section 3, we introduce the photometric and spectroscopic data used in our research. In Section 4, we present the methodology of deriving atmospheric parameters and elemental abundances. In Section 5, we present results of our detailed abundance analysis of transition disc targets. In Section 6, we correlate the obtained chemical depletion profiles with other parameters of the studied binaries (astrometric, photometric, spectroscopic, pulsational, and orbital parameters) and compare with chemical depletion in young stars and ISM. Finally, in Section 7, we present our conclusions.

## 2 TARGET SAMPLE

In this study, we focus on post-AGB/post-RGB binary stars with disc-type SED<sup>2</sup> of the transition type (see Fig. 1 and Table 1). Kluska et al. (2022) presented seven high-probability ( $W_1 - W_3 > 4.5$ ; category 2) and three moderate-probability ( $2.3 < W_1 - W_3 < 4.5$ ,  $H - K < 0.3$ ,  $[Zn/Ti] > 0.7$  dex; category 3) transition disc candidates in the Galaxy. A mid-IR interferometric study by Corporaal et al. (2023) confirmed the inner gaps in six of these Galactic candidates – hence, they are referred to as transition disc stars (see targets #1–#6 in Table 1). The remaining subsample of transition disc targets (targets #7–#10) are referred to as transition disc candidates for the rest of the paper.

We complemented the Galactic subsample of transition disc targets with two moderate-probability transition disc candidates (targets #11 and #12) in the Large Magellanic Cloud (LMC) following the procedure outlined in Kluska et al. (2022). In brief, we used the near-IR colours ( $H - K$  from 2MASS; Skrutskie et al. 2006) and mid-IR colours ( $W_1 - W_3$  from WISE; Wright et al. 2010) to select new targets from the overall sample of post-AGB/post-RGB binary stars with disc-type SEDs in the Small Magellanic Cloud (SMC) (Kamath et al. 2014) and in the LMC (Kamath et al. 2015). From all SMC and LMC targets in categories 2 and 3, we selected those for which high-resolution optical spectra were available (see Fig. 1).

We note that we excluded SS Lep and V777 Mon (Red Rectangle) from our preliminary sample despite their high

mid-IR excesses because of the large corresponding uncertainties ( $(W_1 - W_3)_{SS\ Lep} = 4.76 \pm 0.39$  mag,  $(W_1 - W_3)_{V777\ Mon} = 4.53 \pm 0.35$  mag) as compared to the other 12 targets, which had the uncertainty in  $W_1 - W_3$  below 0.08 mag. We also note that transition disc candidates AF Crt (#8) and V1504 Sco (#10) are observed edge-on (Van Winckel et al. 2012; Kluska et al. 2022), which makes their luminosity estimates (see Section 3.2) less reliable. Nevertheless, despite high inclinations, the depletion profiles of AF Crt (#8) and V1504 Sco (#10) are similar to those of other transition disc targets.

Our final sample consists of 12 transition disc targets: six confirmed transition disc stars (all in the Galaxy) and six transition disc candidates (four in the Galaxy and two in the LMC). We note that the surface composition of all 12 targets in our sample was previously studied by different groups using different methods (see Table 2). In this study, we perform a homogeneous analysis of our targets within the context of disc-binary interaction, accounting for NLTE effects, and re-define depletion efficiency in post-AGB/post-RGB binaries with transition discs. We also note that all targets are Type II Cepheid variables, which allowed us to calculate their luminosities using period-luminosity-colour (PLC) relation (see Section 3.2). We present the target details individually in Appendix A.

## 3 DATA AND OBSERVATIONS

In this section, we present the photometric data (see Section 3.1) used to derive luminosities of transition disc targets. The luminosities were derived using SED fitting and PLC relation for Type II Cepheids (see Section 3.2). We also present the spectroscopic data used to calculate atmospheric parameters and elemental abundances (see Section 3.3).

### 3.1 Photometric data

To obtain the SEDs of our target sample (see Appendix B), we followed the procedure originally developed by Degroote et al. (2013) and recently presented in Mohorian et al. (2024). In brief, we collected the photometric magnitudes across various wavelength bands, which span from optical to far-infrared (far-IR; see Table B1), including data from Johnson-Cousins system (Johnson & Morgan 1953; Cousins 1976), Tycho-2 catalogue (Høg et al. 2000), Sloan Digital Sky Survey (SDSS, York et al. 2000), Two Micron All Sky Survey (2MASS; Skrutskie et al. 2006), WISE (Wright et al. 2010), AKARI (Ishihara et al. 2010), Infrared Astronomical Satellite (IRAS; Neugebauer et al. 1984), Photodetector Array Camera and Spectrometer (PACS; Poglitsch et al. 2010), and Spectral and Photometric Imaging Receiver (SPIRE; Griffin et al. 2010). In Appendix B, we present the SEDs of transition disc targets, fitted with updated *Gaia* DR3 distances (see Section 3.2).

### 3.2 Determination of luminosities from SED fitting and PLC relation

In this study, we determined the luminosities of the target sample using two methods: i) through SED fitting (referred

<sup>2</sup> The disc-type SED is characteristic of the binarity of the host star (Gezer et al. 2015; Kamath et al. 2016; Oomen et al. 2018; Kluska et al. 2022).

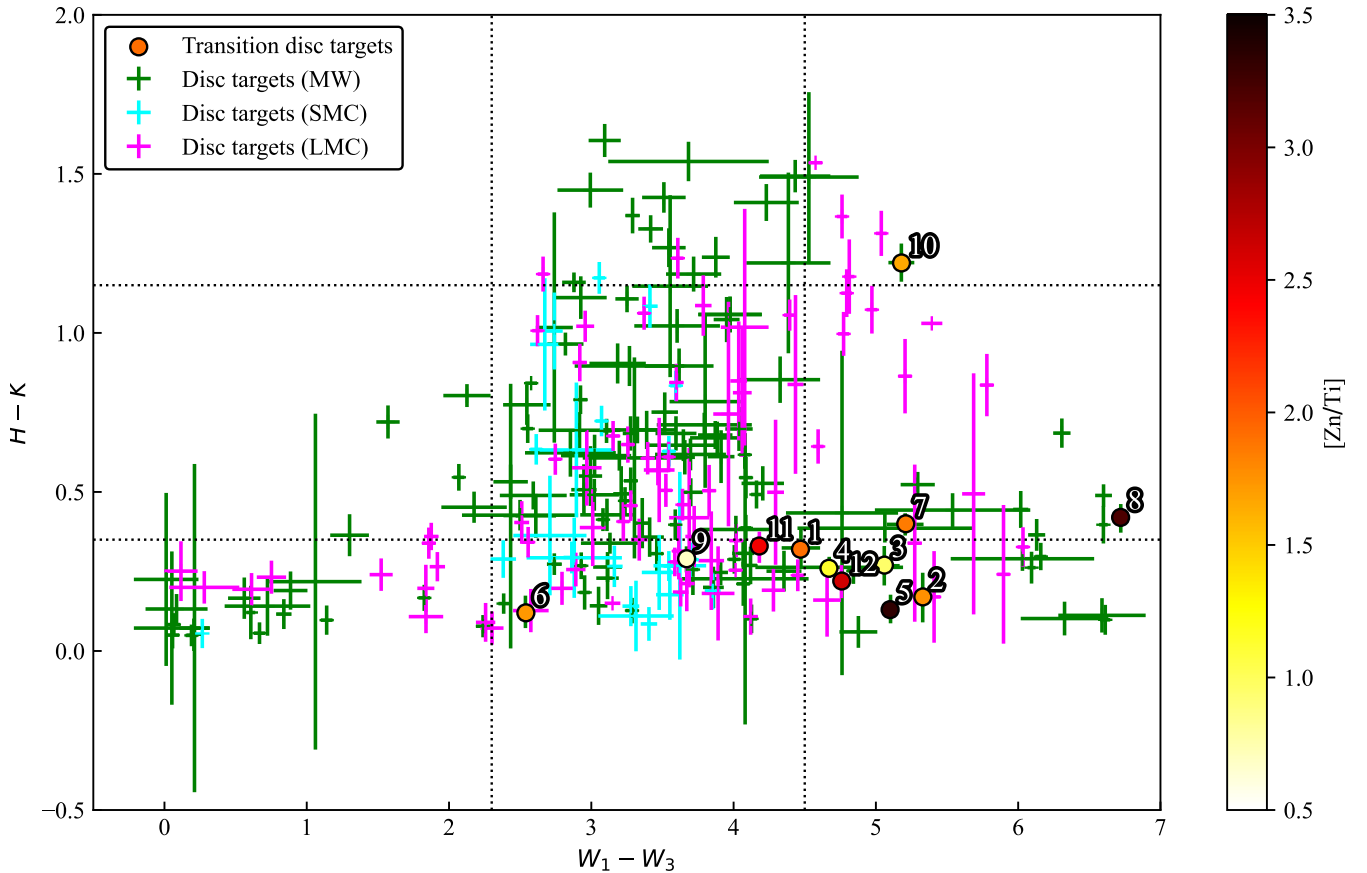


**Figure 1.** Updated IR colour-colour plot of post-AGB/post-RGB binary stars in the Galaxy and in the Magellanic Clouds. NIR magnitudes ( $H$  and  $K$ ) are adopted from 2MASS 6X, while MIR magnitudes ( $W_1$  and  $W_3$ ) are adopted from AllWISE (for more details, see Section 2). Grey error bars represent disc targets in the Galaxy (Kluska et al. 2022), green error bars represent disc targets in the SMC (Kamath et al. 2014), blue error bars represent disc targets in the LMC (Kamath et al. 2015). Our sample of transition disc targets is marked with circles coloured by  $[Zn/Ti]$  abundance ratios from this study (see Table 5). Adopted contours represent the rough demarcation between different disc categories (Kluska et al. 2022).

to as SED luminosity,  $L_{SED}$ ) following the methodology outlined in Mohorian et al. (2024); and ii) employing the PLC relation (referred to as PLC luminosity,  $L_{PLC}$ ) following the procedure outlined in Menon et al. (2024). In this subsection, we provide a brief overview of these methods. In Table 3, we present the estimated SED and PLC luminosities.

To determine the SED luminosities, we selected appropriate Kurucz model atmospheres (Castelli & Kurucz 2003) to fit the initial photometric data points (the bolometric IR luminosity  $L_{IR}$  was obtained through integration of star-subtracted IR excess) and computed the de-reddened model atmospheres for each target through an extensive parameter grid search (Mohorian et al. 2024). The search was performed by the minimisation of the  $\chi^2$  value in the parameter space of four variables: effective temperature  $T_{eff}$ , surface gravity  $\log g$ , total reddening (extinction parameter)  $E(B - V)$ , and angular diameter of the star  $\theta$ . The total reddening comprised both interstellar and circumstellar contributions. For interstellar reddening, we adopted the wavelength-dependent extinction law (Cardelli et al. 1989), assuming an  $R_V = 3.1$ . Additionally, we used the Bailer-Jones geometric distances, denoted as  $z_{BJ}$ , along with their corresponding lower and upper limits,  $z_{BJL}$  and  $z_{BJU}$  (Bailer-Jones et al. 2021). These more precise geometric distances were computed based on *Gaia*

DR3 parallaxes, incorporating a direction-dependent prior distance. We note that throughout our computations, we assumed isotropic radiation emission from the stars. We also note that stellar variability was not accounted for, resulting in an increased  $\chi^2$  value for high-amplitude variables. Once the solution for the de-reddened model atmosphere was found, we integrated it to obtain the SED luminosity  $L_{SED}$  and the relative bolometric IR luminosity  $L_{IR}/L_* = L_{IR}/L_{SED}$ . The luminosity uncertainties were derived for each respective target by computing the standard deviation of the lower and upper luminosity bounds, caused by uncertainties of the geometric distances and the photometric data points.

To derive the PLC luminosity, we used the calibrated relation (Menon et al. 2024) given by

$$M_{bol} = m \times \log P_0 + c - \mu + BC + 2.55 \times (V - I)_0, \quad (1)$$

where  $M_{bol}$  represents the absolute bolometric magnitude obtained using Wesenheit (colour-corrected) V-band magnitude ( $WI_V = V - 2.55(V - I)_0$ ; see Ngeow & Kanbur 2005), while the parameters  $m = -3.59$  and  $c = 18.79$  correspond to the calibrated slope and intercept of the linear fit, respectively.  $P_0$  represents the observed fundamental pulsation period in days,  $\mu = 18.49$  denotes the distance modulus to the LMC,  $BC$  signifies the bolometric correction derived from the ef-



**Table 1.** Names, coordinates, and selection criteria of the target sample (see Section 2).  $H$  and  $K$  magnitudes were adopted from the 2MASS 6X catalogue;  $W_1$  and  $W_3$  magnitudes were adopted from the AllWISE catalogue.  $[\text{Zn}/\text{Ti}]$  abundance ratio is a proxy for the efficiency of depletion process (see Section 1).

ID	IRAS/OGLE	Names		Coordinates		Selection criteria		
		2MASS	Variable	R.A. (deg)	Dec. (deg)	$H - K$ (mag)	$W_1 - W_3$ (mag)	$[\text{Zn}/\text{Ti}]$ (dex)
Transition disc stars (Corporaal et al. 2023)								
1	06072+0953	J06095798+0952318	CT Ori	092.491630	+09.875519	0.324	4.473	1.9 <sup>a</sup>
2	06472-3713	J06485640-3716332	ST Pup	102.235100	-37.275900	0.168	5.329	2.1 <sup>b</sup>
3	12067-4508	J12092381-4525346	RU Cen	182.348800	-45.426400	0.268	5.059	1.0 <sup>c</sup>
4	18281+2149	J18301623+2152007	AC Her	277.567500	+21.866670	0.263	4.672	0.7 <sup>d</sup>
5	18564-0814	J18590869-0810140	AD Aql	284.786283	-08.170671	0.132	5.103	2.5 <sup>d</sup>
6	19163+2745	J19181955+2751031	EP Lyr	289.581300	+27.850890	0.123	2.537	1.3 <sup>e</sup>
Transition disc candidates (categories 2 and 3 in Kluska et al. 2022)								
7	06034+1354	J06061490+1354191	DY Ori	091.562130	+13.905310	0.398	5.206	2.1 <sup>e</sup>
8	11472-0800	J11494804-0817204	AF Crt	177.450151	-08.289059	0.417	6.721	3.4 <sup>f</sup>
9	16278-5526	J16315414-5533074	GZ Nor	247.975624	-55.552108	0.288	3.669	0.8 <sup>g</sup>
10	17233-4330	J17265864-4333135	V1504 Sco	261.744331	-43.553756	1.221	5.179	1.4 <sup>h</sup>
11	LMC-029 <sup>1</sup>	J05030498-6840247	LMC V0770	075.770630	-68.673500	0.326	4.181	2.3 <sup>i</sup>
12	LMC-147 <sup>1</sup>	J05315099-6911463	LMC V3156	082.962495	-69.196213	0.218	4.758	2.5 <sup>j</sup>

**Notes:** <sup>1</sup>OGLE names of two LMC targets were shortened from OGLE LMC-T2CEP-029 and OGLE LMC-T2CEP-147 to LMC-029 and LMC-147, respectively. The superscripts of the  $[\text{Zn}/\text{Ti}]$  values indicate the individual chemical abundance studies: <sup>a</sup>Gonzalez et al. (1997b); <sup>b</sup>Gonzalez & Wallerstein (1996); <sup>c</sup>Maas et al. (2002); <sup>d</sup>Giridhar et al. (1998); <sup>e</sup>Gonzalez et al. (1997a); <sup>f</sup>Van Winckel et al. (2012); <sup>g</sup>Gezer et al. (2019); <sup>h</sup>Maas et al. (2005); <sup>i</sup>Kamath & Van Winckel (2019); <sup>j</sup>Reyniers & van Winckel (2007).

**Table 2.** Literature data on photometric parameters, orbital parameters, luminosity estimates, and depletion parameters of transition disc targets (see Section 2).

ID	Name	Photometric parameters		Orbital parameters		Previous luminosity estimates			Depletion parameters	
		RVb	$P_{\text{puls}}$ (d)	$P_{\text{orb}}$ (d)	$e$	$L_{\text{SED}}$ ( $L_{\odot}$ )	$L_{\text{PLC}}$ ( $L_{\odot}$ )	$L_{\text{IR}}/L_{\ast}$	$T_{\text{turn-off}}$ (K)	Profile
1	CT Ori	no	33.65 <sup>f</sup>	-	-	15100 <sup>c</sup>	-	0.55 <sup>d</sup>	1200	S
2	ST Pup	no	18.73 <sup>e</sup>	406 <sup>b</sup>	0.00 <sup>b</sup>	690 <sup>c</sup>	-	0.72 <sup>d</sup>	800	S
3	RU Cen	no	32.37 <sup>g</sup>	1489 <sup>b</sup>	0.62 <sup>b</sup>	1100 <sup>c</sup>	-	0.40 <sup>d</sup>	800	P
4	AC Her	no	37.73 <sup>h</sup>	1189 <sup>b</sup>	0.00 <sup>b</sup>	2400 <sup>c</sup>	3600 <sup>i</sup>	0.21 <sup>d</sup>	1200	U
5	AD Aql	no	32.7 <sup>h</sup>	-	-	11500 <sup>c</sup>	-	0.51 <sup>d</sup>	1000	S
6	EP Lyr	no	41.59 <sup>g</sup>	1151 <sup>b</sup>	0.39 <sup>b</sup>	5500 <sup>c</sup>	7100 <sup>i</sup>	0.02 <sup>d</sup>	800	P
7	DY Ori	no	30.155 <sup>a</sup>	1248 <sup>b</sup>	0.22 <sup>b</sup>	21500 <sup>c</sup>	-	0.55 <sup>d</sup>	1000	U
8	AF Crt	no	31.5 <sup>f</sup>	-	-	280 <sup>c</sup>	-	1.83 <sup>d</sup>	1000	S
9	GZ Nor	no	36.2 <sup>l</sup>	-	-	1400 <sup>c</sup>	-	0.22 <sup>d</sup>	800	P
10	V1504 Sco	yes	22.0 <sup>f</sup>	735 <sup>f</sup>	-	1100 <sup>c</sup>	-	4.69 <sup>d</sup>	1000	S
11	LMC V0770	no	31.245 <sup>j</sup>	-	-	3300 <sup>m</sup>	2629 <sup>j</sup>	0.63 <sup>k</sup>	-	-
12	LMC V3156	no	46.795 <sup>j</sup>	-	-	5900 <sup>j</sup>	6989 <sup>j</sup>	0.84 <sup>k</sup>	-	-

**Notes:** Literature data on depletion profiles is adopted from Oomen et al. (2019): ‘S’ means ‘saturated’, ‘P’ means ‘plateau’, ‘U’ means ‘uncertain’. The source list: <sup>a</sup>Pawlak et al. (2019), <sup>b</sup>Oomen et al. (2018), <sup>c</sup>Oomen et al. (2019), <sup>d</sup>Kluska et al. (2022), <sup>e</sup>Walker et al. (2015), <sup>f</sup>Kiss et al. (2007), <sup>g</sup>Bódi & Kiss (2019), <sup>h</sup>Giridhar et al. (1998), <sup>i</sup>Bollen et al. (2022), <sup>j</sup>Manick et al. (2018), <sup>k</sup>van Aarle et al. (2011), <sup>l</sup>Gezer et al. (2019), <sup>m</sup>Kamath et al. (2015).

fective temperature (Flower 1996; Torres 2010), and  $(V - I)_0$  denotes the intrinsic (de-reddened) colour of each star (reddening value is adopted from SED fits). The uncertainties of PLC luminosity are primarily influenced by the uncertainties of reddening.

We note that SED luminosities require *Gaia* parallax measurements (underlying the derivation of geometric distances), which are plagued by orbital motion in case of binary systems (Kluska et al. 2022). Additionally, since the targets in this study are Type II Cepheid pulsating variables with periods ranging from 18.73 to 46.7 days (see Table 2), their atmo-

spheric parameters, particularly effective temperature  $T_{\text{eff}}$ , surface gravity  $\log g$ , and microturbulent velocity  $\xi_t$ , undergo significant variations throughout the pulsation cycle (Mohorian et al. 2024). This causes a considerable scatter in the photometric data points leading to increased uncertainties of SED luminosity (see Appendix B). Hence, we regard the PLC luminosity to be more precise and reliable compared to the SED luminosity in our targets.

**Table 3.** Derived luminosities and atmospheric parameters of transition disc targets. The columns are as follows: col. 1: Target ID; col. 2: Target name; col. 3: SED luminosity (see Section 3.2); col. 4: infrared luminosity; col. 5: PLC luminosity (adopted; see Section 3.2); col. 6, 7, 8, 9: derived atmospheric parameters (see Section 5.1).

ID	Name	$\log \frac{L_{\text{SED}}}{L_{\odot}}$	$\log \frac{L_{\text{IR}}}{L_{\text{SED}}}$	$\log \frac{L_{\text{PLC}}}{L_{\odot}}$	$T_{\text{eff}}$ (K)	$\log g$ (dex)	[Fe/H] (dex)	$\xi_t$ (km/s)
1	CT Ori	3.41±0.13	-0.26±0.13	3.26±0.16	5940±120	1.01±0.18	-1.89±0.11	3.37±0.10
2	*ST Pup	2.87±0.08	-0.14±0.08	2.96±0.17	5340±80	0.20±0.10	-1.92±0.08	2.83±0.03
3	RU Cen	4.00±0.22	-0.40±0.22	3.50±0.27	6120±80	1.46±0.15	-1.93±0.08	3.26±0.10
4	AC Her	3.79±0.11	-0.68±0.11	3.71±0.21	6140±100	1.27±0.16	-1.47±0.08	3.92±0.12
5	AD Aql	3.41±0.19	-0.29±0.19	2.84±0.29	6200±170	1.67±0.45	-2.20±0.09	2.98±0.36
6	EP Lyr	3.74±0.16	-1.70±0.16	3.96±0.23	6270±160	1.24±0.18	-2.03±0.17	2.48±0.10
7	*DY Ori	2.81±0.10	-0.26±0.13	3.50±0.17	6160±70	0.88±0.14	-2.03±0.04	2.48±0.09
8	*AF Crt	–	0.26±0.08	2.51±0.17	6110±110	0.96±0.21	-2.47±0.05	4.87±0.16
9	*GZ Nor	3.24±0.15	-0.66±0.22	2.71±0.29	4830±20	0.00±0.18	-1.89±0.11	5.95±0.18
10	V1504 Sco	–	0.67±0.11	3.71±0.35	5980±90	0.98±0.17	-1.05±0.07	4.29±0.05
11	*LMC V0770	3.42±0.11	-0.20±0.19	3.46±0.20	5750±100	0.00±0.18	-2.61±0.05	2.20±0.01
12	*LMC V3156	3.75±0.08	-0.08±0.16	3.99±0.19	6160±130	1.38±0.20	-2.48±0.04	4.28±0.12

**Notes:** We highlight with asterisks (\*) those targets, for which we used the ATLAS9 model atmospheres (see Section 4.1). For the uncertainty of infrared luminosity, we assume that the error of SED luminosity, primarily due to reddening uncertainty, dominates over the error from fitting the infrared bump, which is influenced by the uncertainty in photometric data points. SED luminosities of edge-on targets AF Crt (#8) and V1504 Sco (#10) were removed from the table as SED fitting is not applicable when the optical light is dominated by scattering.

### 3.3 Spectroscopic data

In this subsection, we present the optical high-resolution spectra used in this study, which were obtained from the High Efficiency and Resolution Mercator Echelle Spectrograph mounted on Mercator telescope (HERMES/Mercator; see Section 3.3.1) and Ultraviolet and Visual Echelle Spectrograph mounted on Very Large Telescope (UVES/VLT; see Section 3.3.2). In Table 4, we present the final selection of spectral visits (for all considered visits, see Appendix C). In Fig. 2, we show exemplary spectral regions for all targets, focusing on the S and Zn lines, which are crucial for deriving the initial metallicity  $[M/H]_{0,\text{min}}$ , because Fe is depleted in transition disc targets (see Section 4).

To ensure the accuracy of the abundance analysis of the pulsating transition disc targets, our selection of optical visits depended on the time span of observational dataset for each target. Our selection strategy is as follows (see Table 4):

(i) ST Pup (#2), RU Cen (#3), GZ Nor (#9), V1504 Sco (#10): We used the only available spectrum for each of these targets.

(ii) LMC V3156 (#11) and LMC V0770 (#12): Multiple spectra of these targets were taken in less than two-day span (1.08 days and 0.07 days, respectively). Since the pulsation periods of these targets are greater than 30 days, we merged the RV-corrected spectra of each target to increase the S/N ratio.

(iii) CT Ori (#1), AC Her (#4), AD Aql (#5), EP Lyr (#6), DY Ori (#7), and AF Crt (#8): These targets are part of long-term spectral monitoring program using HERMES (see Section 3.3.1). Since the observations of these targets were generally taken with a gap of at least few days, we selected the individual visits of these targets with the highest S/N values.

**Table 4.** Observation log of the target sample. For more information on the selection criteria for the spectral visits, see Section 2. In Appendix C, we provide the full observational log of transition disc targets.

ID	Name	Facility	MJD	RV (km/s)	S/N
1	CT Ori	H/M	56254.1414	47.12±0.96	45
2	ST Pup	H/M	51085.2822	23.03±0.38	50
3	RU Cen	H/M	51627.1188	-0.40±0.28	55
4	AC Her	H/M	57876.1807	-54.18±0.57	45
5	AD Aql	H/M	56870.9410	54.36±0.96	40
6	EP Lyr	H/M	55005.1064	29.37±1.29	45
7	DY Ori	H/M	58452.1440	11.67±0.90	40
8	AF Crt	H/M	56298.2332	27.72±1.08	40
9	GZ Nor	U/V	56819.4194	-121.61±0.26	50
10	V1504 Sco	H/M	51626.3207	28.43±0.25	50
11	LMC V0770	U/V	56589.1761	288.96±3.37	45
12	LMC V3156	U/V	53409.9187	280.06±1.26	45

**Notes:** H/M means HERMES/Mercator, U/V means UVES/VLT. RV is the radial velocity of the spectrum used in the analyses. S/N is the average signal-to-noise ratio of the spectrum.

#### 3.3.1 HERMES spectra

For CT Ori (#1), ST Pup (#2), RU Cen (#3), AC Her (#4), AD Aql (#5), EP Lyr (#6), DY Ori (#7), AF Crt (#8), and V1504 Sco (#10), we used the high-resolution ( $R = \lambda/\Delta\lambda \sim 85\,000$ ) optical spectra obtained within an extensive monitoring initiative (June 2009–ongoing). This initiative involved HERMES (Raskin et al. 2011) installed on the 1.2-m Mercator telescope at the Roque de los Muchachos Observatory, La Palma.

This monitoring program resulted in the collection of a substantial dataset of high-resolution optical spectra for post-AGB systems, thoroughly detailed in Van Winckel (2018). The HERMES spectra of transition disc targets were re-

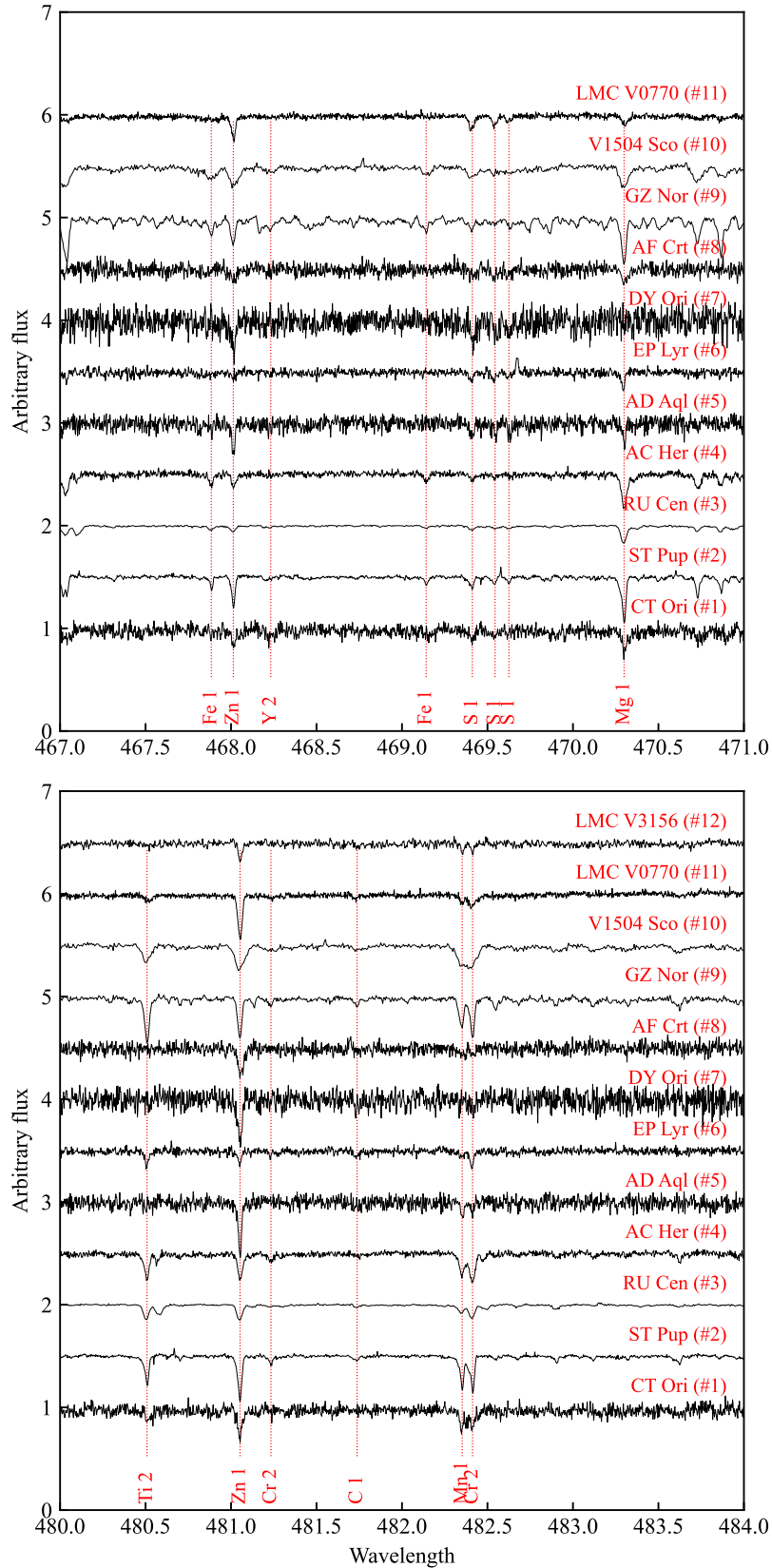


**Figure 2.** Comparison of the normalised spectra of all sample stars in two spectral regions containing lines of volatile elements S and Zn. All spectra are normalised, corrected for radial velocity, and shifted in flux for clarity. The dashed red vertical lines indicate positions of line peaks. The names of the stars are provided in the plot. The observed spectrum of LMC V3156 does not contain the region between 467.5 and 470.5 nm (for more details, see Section 3.3).

duced using the standard pipeline, as outlined in [Raskin et al. \(2011\)](#). The complete log of HERMES observations can be found in Appendix C, with the selected visits listed in Table 4.

### 3.3.2 UVES spectra

For GZ Nor (#9), LMC V0770 (#11), and LMC V3156 (#12) we employed high-resolution optical spectra ( $R = \lambda/\Delta\lambda \sim 80\,000$  in the Blue arm;  $R = \lambda/\Delta\lambda \sim 110\,000$  in the Red arm) obtained with the UVES ([Dekker et al. 2000](#)). UVES is mounted on the 8-m UT2 Keuyen Telescope at the VLT located at the Paranal Observatory of ESO in Chile.

To reduce the UVES spectra, we followed the standard steps for UVES reduction pipeline (frame extraction, flat-field correction, wavelength calibration, cosmic clipping; see [Dekker et al. 2000](#)). The full observational log of UVES spectra can be found in Appendix C, and the selected visits are listed in Table 4.

## 4 SPECTRAL ANALYSIS

In this study, we used E-iSpec (explained in detail in [Mohorian et al. 2024](#)) – a modified version of iSpec ([Blanco-Cuaresma et al. 2014](#); [Blanco-Cuaresma 2019](#)) to investigate the chemical composition of the target sample. Our chemical analysis included precise derivation of atmospheric parameters (effective temperature  $T_{\text{eff}}$ , surface gravity  $\log g$ , metallicity  $[\text{Fe}/\text{H}]$ , and microturbulent velocity  $\xi_t$ ) and abundances  $[\text{X}/\text{H}]$  of all elements, which had detectable spectral features in the spectra of transition disc targets. Additionally, we used **Balder** ([Amarsi et al. 2018a](#)) to calculate NLTE corrections for the abundances of a representative set of 11 chemical elements: C, N, O, Na, Mg, Al, Si, S, K, Ca, and Fe. In the following subsections, we present the methodology of abundance analysis of transition disc stars and candidates (for individual depletion profiles, see Appendix E).

### 4.1 LTE analysis using E-iSpec

To calculate the atmospheric parameters and elemental abundances from atomic spectral lines, we followed the procedure presented in [Mohorian et al. \(2024\)](#). In brief, we used the Moog radiative transfer code (equivalent width method; [Snedden 1973](#)) with the VALD3 line list ([Kupka et al. 2011](#)), the recently updated solar abundances from [Asplund et al. \(2021\)](#), and LTE model atmospheres: spherically-symmetric MARCS models ([Gustafsson et al. 2008](#)) and plane-parallel ATLAS9 models ([Castelli & Kurucz 2003](#))<sup>3</sup>.

In the original version of E-iSpec ([Mohorian et al. 2024](#)), the uncertainties were calculated manually. In this study, we updated E-iSpec by automating the process of uncertainty calculation for elemental abundances, while following the same approach as in manual method. In brief, the total

uncertainty is calculated as the sum in quadrature of random and systematic uncertainties. We note that we set the random uncertainty to be 0.1 dex for those ionisations, for which we used only one spectral line to derive the elemental abundance. We assume that the abundance change caused by metallicity affects  $[\text{X}/\text{Fe}]$ , but does not affect  $[\text{X}/\text{H}]$ . In Fig. 3 and 4, we show the derived elemental abundances with uncertainties for all transition disc stars and candidates, respectively. Furthermore, we updated E-iSpec with a functionality to recalculate atmospheric parameters and elemental abundances using NLTE abundance corrections from **Balder** (see Section 4.2).

In Table 3, we present the estimated SED and PLC luminosities (see Section 3.2) and the derived atmospheric parameters of the target sample (the targets, for which we used ATLAS9 model atmospheres, are highlighted with asterisks). In Tables 5 and E1, we provide the results of our abundance analysis using E-iSpec: the selected abundance ratios and the elemental abundances, respectively all 12 targets is provided in Appendix D.

### 4.2 NLTE abundance corrections using Balder

The departures from LTE typically (but not always) grow with increasing temperature  $T_{\text{eff}}$ , decreasing surface gravity  $\log g$ , or decreasing metallicity  $[\text{Fe}/\text{H}]$  ([Lind et al. 2012](#)). These departures primarily stem from the intense radiation field at shorter wavelengths, which is not effectively compensated by thermal collisions in the stellar photosphere. Among the various species, neutral and relatively low-ionisation elements like Fe I or Ti I experience overionisation, resulting in weakened spectral lines. Conversely, the dominant ionisation stage like Fe II or Ti II closely follows the Saha distribution, and remains mostly unaffected by NLTE effects ([Amarsi et al. 2016b, 2022](#)). Thus, we adopted  $[\text{Fe}/\text{H}]$  abundance derived from Fe II lines as the metallicity and applied NLTE corrections to elemental abundances (see [Amarsi et al. 2020b](#), and references therein).

To study the chemical depletion in post-AGB/post-RGB binary stars with transition discs, we selected C, N, O, Na, Mg, Al, Si, S, K, Ca, and Fe as a representative set of chemical elements. We calculated the NLTE corrections for each individual studied spectral line of these elements using the code **Balder**, which is based on **Multi3D** ([Leenaarts & Carls-son 2009](#)).

The method of NLTE correction calculation closely follows that described in [Amarsi et al. \(2020b\)](#). We list the model atoms used in this work in Table 6. The NLTE calculations were performed on a small number of LTE spherically-symmetric MARCS model atmospheres ([Gustafsson et al. 2008](#)) using two small grids: the hotter grid spanned  $5\,500\text{ K} \leq T_{\text{eff}} \leq 6\,250\text{ K}$ ,  $1.0\text{ dex} \leq \log g \leq 2.0\text{ dex}$ , and  $-2.5\text{ dex} \leq [\text{Fe}/\text{H}] \leq -1.0\text{ dex}$ , while the cooler grid spanned  $4\,750\text{ K} \leq T_{\text{eff}} \leq 5\,250\text{ K}$ ,  $\log g = 0.5\text{ dex}$ , and  $-2.0\text{ dex} \leq [\text{Fe}/\text{H}] \leq -1.5\text{ dex}$ . Calculations were performed for a range of abundances from  $[\text{X}/\text{H}] = -4.5$  to  $+2.0$  in steps of 0.5 dex, and microturbulences  $\xi_t = 2.0\text{ km/s}$  and  $5.0\text{ km/s}$ . The theoretical equivalent widths were used to calculate NLTE abundance corrections for each individual spectral line  $i$ , denoted as  $\Delta_i^{\text{diff}}$ . These were interpolated onto the stellar parameters of interest, with edge values adopted for stars outside of this theoretical grid. The resulting line-by-line NLTE abundances

<sup>3</sup> In general, spherically-symmetric models are known to perform better for giant stars due to their extended atmospheres ([Mészáros et al. 2012](#)). However, half of our target sample had atmospheric parameters outside of MARCS parameter grid values; for such targets we used the ATLAS9 model atmospheres instead.



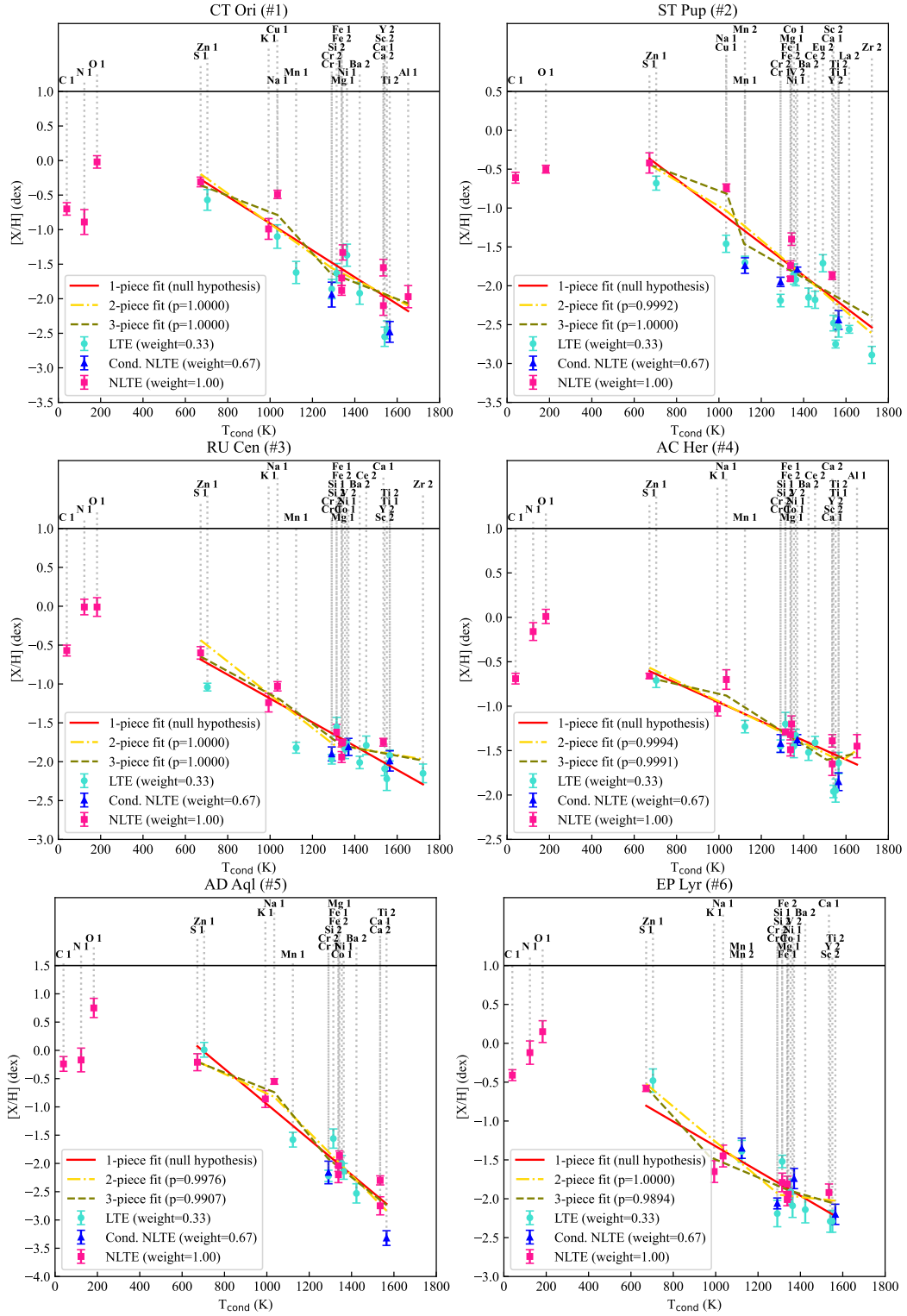


**Figure 3.** Elemental abundances of transition disc stars (CT Ori, ST Pup, RU Cen, AC Her, AD Aql, and EP Lyr) as functions of condensation temperature (Lodders 2003; Wood et al. 2019). The legend for the symbols and colours used is included within the plot. “Cond. NLTE” means conditionally NLTE abundance (derived from spectral lines of Ti II, V II, Cr II, or Mn II; for more details, see Section 5.1).

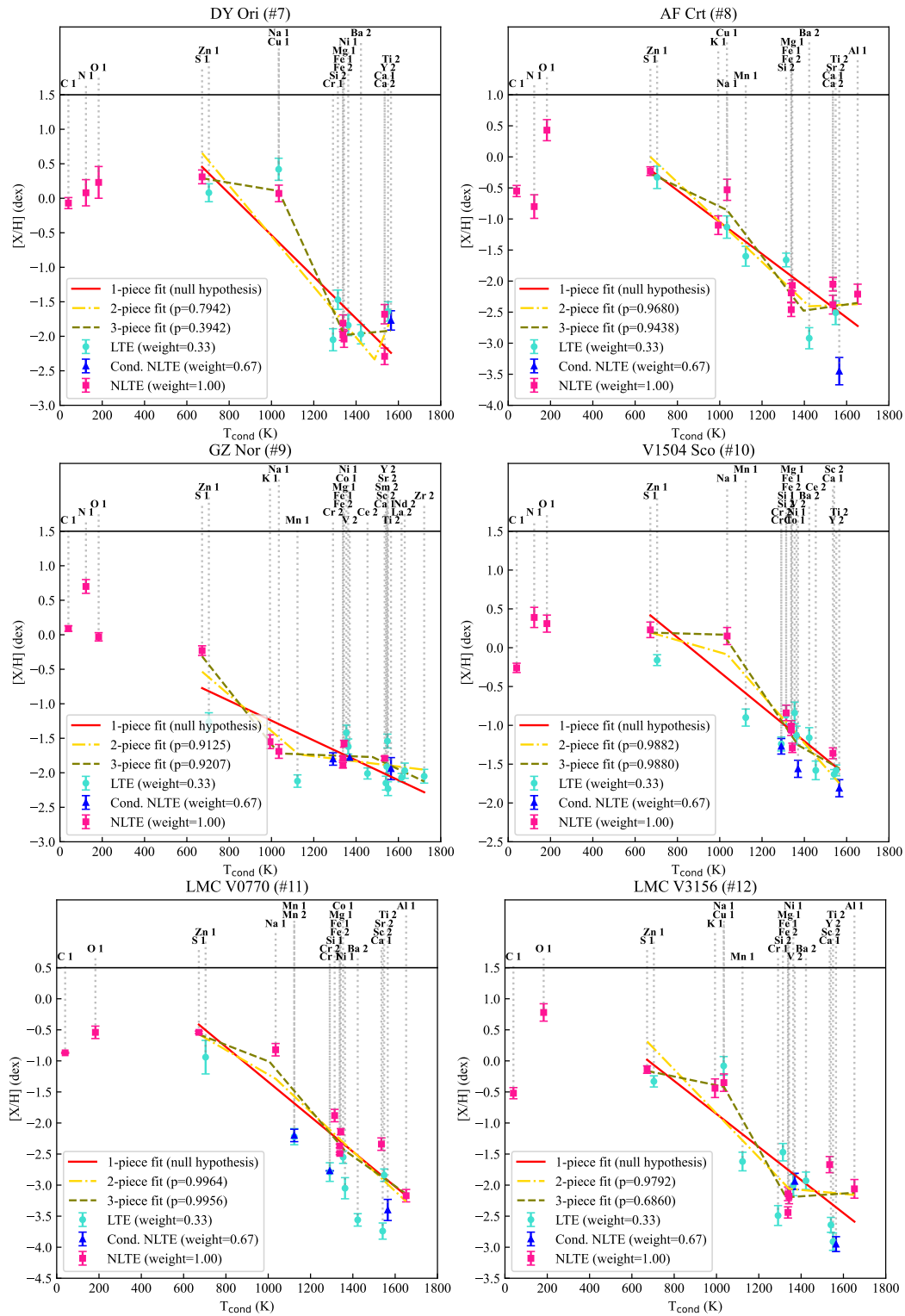


**Figure 4.** Elemental abundances of transition disc candidates (DY Ori, AF Crt, GZ Nor, V1504 Sco, LMC V0770, and LMC V3156) as functions of condensation temperature (Lodders 2003; Wood et al. 2019). The legend for the symbols and colours used is included within the plot. “Cond. NLTE” means conditionally NLTE abundance (derived from spectral lines of Ti II, V II, Cr II, or Mn II; for more details, see Section 5.1).

**Table 5.** Selected abundance ratios of transition disc targets (see Table E1 for a full list of [X/H] abundances). The columns are as follows: col. 1: Target ID; col. 2: Target name; col. 3, 4, 5: proxies for depletion efficiency (we adopt the NLTE-corrected [S/Ti] ratio, see Section 5.2); col. 6: NLTE-corrected C/O ratio; col. 7: minimal initial metallicity (see Section 5.2); col. 8: depletion strength (see Section 6.2).

ID	Name	LTE [Zn/Ti] (dex)	LTE [Zn/Fe] (dex)	NLTE [S/Ti] (dex)	NLTE C/O	NLTE [M/H] <sub>0,min</sub> (dex)	NLTE $\Delta_{g/d}$
1	CT Ori	1.91±0.30	1.31±0.23	2.17±0.25	0.12±0.04	-0.31±0.10	3720
2	ST Pup	1.76±0.21	1.23±0.15	2.02±0.35	0.46±0.11	-0.42±0.23	3090
3	RU Cen	0.95±0.18	0.90±0.14	1.39±0.28	0.16±0.06	-0.60±0.15	2190
4	AC Her	1.14±0.18	0.78±0.18	1.19±0.14	0.12±0.03	-0.66±0.04	680
5	AD Aql	3.33±0.26	2.21±0.28	3.11±0.34	0.06±0.03	-0.21±0.21	9770
6	EP Lyr	1.72±0.28	1.53±0.31	1.62±0.20	0.16±0.06	-0.58±0.07	2690
7	DY Ori	1.85±0.27	2.06±0.22	2.08±0.35	0.30±0.15	0.31±0.21	19500
8	AF Crt	3.12±0.40	2.13±0.30	3.22±0.31	0.06±0.03	-0.23±0.09	16980
9	GZ Nor	0.68±0.29	0.63±0.22	1.71±0.28	0.78±0.16	-0.23±0.12	4570
10	V1504 Sco	1.65±0.18	0.90±0.20	2.04±0.11	0.16±0.05	0.23±0.00	1950
11	LMC V0770	2.46±0.44	1.55±0.32	2.86±0.19	0.28±0.06	-0.54±0.02	8910
12	LMC V3156	2.62±0.21	2.11±0.19	2.81±0.19	0.03±0.01	-0.14±0.07	19950

were given by:

$$[X/H]_i^{\text{NLTE}} = [X/H]_i^{\text{LTE}} + \Delta_i^{\text{diff.}}, \quad (2)$$

where superscript “diff.” highlights that we use the relative abundance scale [X/H], which requires  $\Delta_i^{\text{diff.}}$  to also include the NLTE corrections to the solar absolute abundances of the corresponding elements. We note that we assume the differences between the ATLAS9 model atmospheres (used for a subsample of targets) and the MARCS models (used in NLTE calculations) to be of secondary importance compared to the total uncertainties of the LTE abundances as well as the uncertainties of the NLTE models. For the uncertainties of NLTE abundances, we assume the same systematic component as in the LTE abundances, and recalculate the random component in similar way (for one spectral line,  $\sigma_{\text{random}} = 0.1$  dex; for more spectral lines  $\sigma_{\text{random}}$  is the standard deviation).

## 5 ELEMENTAL ABUNDANCES OF TRANSITION DISC TARGETS

In this section, we present the results of our LTE and NLTE abundance analysis of optical spectra of transition disc targets (see Section 5.1), define depletion indicators used for our sample (see Section 5.2), and compare derived depletion profiles with those from previous studies (see Section 5.3).

### 5.1 Observed depletion profiles

In Fig. 3 and 4, we present the depletion patterns together with the corresponding fits for each target. We mark elemental abundances corrected for NLTE effects with pink squares. For Fe-peak elements beyond the  $\alpha$ -process (from Ti to Fe), we considered the abundances derived from the ionised lines to be likely less sensitive to NLTE effects (i.e., conditionally NLTE; Ti II, V II, Cr II, Mn II). We denote these abundances with blue triangles. We mark the LTE abundances of the all remaining ionisations with light blue circles. The

depletion profiles were fitted from S to Zr based on the arbitrary reliability of the abundance measurement: NLTE abundances were weighted as 1, conditionally NLTE abundances were weighted as 0.67, and LTE abundances were weighted as 0.33. In this approach, the abundance of each ionisation was treated separately, which provided more weight to those elements, for which the abundances of two ionisations were measured. We note that the chosen weighting is an arbitrary measure used to emphasise the difference between fully-LTE depletion profile and NLTE-corrected depletion profile.

One-piece linear fits (red solid lines) represent the homogeneous depletion profile without any break temperatures caused by the onset of depletion ( $T_{\text{turn-off}}$ ) or plateau ( $T_{\text{plateau}}$ ). Two-piece and three-piece linear fits (yellow dashed-dotted and green dashed lines, respectively) represent the depletion with any or both of these break temperatures, respectively. Two-piece and three-piece fits were tested against the one-piece linear fit (which was considered null hypothesis) using the likelihood ratio test: if the p-value of the two- or three-piece linear fit is less than 0.05, this fit offers significantly better<sup>4</sup> goodness-of-fit for the depletion profile than the one-piece linear fit.

The major differences between LTE and NLTE-corrected abundances in transition disc targets are summarised below:

(i) For our targets, NLTE corrections decrease C/O ratio by up to  $\sim 30\%$  (mainly due to NLTE corrections for the high-excitation C I lines used here<sup>5</sup>). However, for GZ Nor (#9), NLTE corrections increase C/O ratio by two times.

(ii) The average line-to-line scatter of NLTE abundances is generally lower than the average line-to-line scatter of LTE abundances, with the most prominent reduction of the scatter

<sup>4</sup> Meaning that the decrease in the  $\chi^2$  value for a more elaborate model is large enough to justify the reduction in degrees of freedom by invoking new constraints (parameters).

<sup>5</sup> For all targets except GZ Nor (#9), the O abundances are based on the low-excitation forbidden [O I] lines that are insensitive to NLTE effects (e.g. (Amarsi et al. 2016a)).

for Na (0.04 dex), Al (0.05 dex), Si (0.07 dex), K (0.04 dex), and Ca (0.04 dex).

(iii) The final depletion profiles of transition disc targets are well-fitted by one-piece linear trends. This result highlights that derived depletion profiles of all transition disc targets are saturated.

(iv) There are few prominent (but statistically insignificant) deviations from one-piece fits of depletion profiles: i) [Na/H] and [Cu/H] in DY Ori (#7), ii) [S/H] in GZ Nor (#9), iii) [Na/H] in V1504 Sco (#10), and iv) [Mn/H] in RU Cen (#3) and GZ Nor (#9). The deviations in [Na/H], [Cu/H], and [S/H] abundances may be caused by the differences in chemical composition and conditions between the transition disc targets and the solar-mixture gas assumed in chemical equilibrium calculations Wood et al. (2019) (especially, for S in the least O-rich transition disc target from our sample,  $C/O_{\text{GZ Nor}} = 0.78$ ). We note that RU Cen (#3) and GZ Nor (#9) clearly show saturation if we temporarily set aside the [Mn/H] abundance. The explanation for this is that the NLTE correction for Mn lines in metal-poor giants generally are positive ( $[\text{Mn}/\text{H}]_{\text{NLTE}} - [\text{Mn}/\text{H}]_{\text{LTE}} \sim +0.6$  dex for  $[\text{Fe}/\text{H}] = -3$  dex; Bergemann & Gehren 2008; Amarsi et al. 2020b), bringing [Mn/H] abundance closer to the linear decline of the depletion profile. We also note that the behaviour of the condensation temperatures for environments with different C/O ratios is out of the scope of this work, though it is a promising path for the future study.

Finally, we also note that an alternative explanation for the enhancement of [Na/H] = 0.15 dex in V1504 Sco involves the first and second dredge-ups, which may be responsible for [Na/H] enhancement in progenitors with intermediate masses  $M_* > 4.5M_{\odot}$  (Karakas & Lattanzio 2014).

## 5.2 Definition and rationale for depletion indicators

To characterise the depletion profiles, we defined  $[\text{S}/\text{H}]_{\text{NLTE}}$  as the lower limit of the initial metallicity  $[\text{M}/\text{H}]_{0,\text{min}}$ , and  $[\text{S}/\text{Ti}]_{\text{NLTE}}$  as the NLTE depletion scale (we use  $[\text{Ti}/\text{H}]_{\text{LTE}}$  derived from Ti II lines as  $[\text{Ti}/\text{H}]_{\text{NLTE}}$ ). Our reasoning for selecting S as volatile indicator and Ti as refractory indicator is as follows:

(i) C, N, and O in post-AGB/post-RGB stars are modified to an unknown extent by the convective and non-convective mixing processes on AGB/RGB, such as dredge-ups (Kobayashi et al. 2011; Ventura et al. 2020; Kamath et al. 2023; Mohorian et al. 2024). Moreover, CNO elements may be partially depleted, as seen in protoplanetary discs, through a poorly constrained process of CO and N<sub>2</sub> molecules (the major carriers of volatile CNO elements in the disc) converting into CO<sub>2</sub> and NH<sub>3</sub> ice and freezing-out onto dust grains (possible explanations include dispersal of gas disc, interactions between the gas and the dust, and chemical reprocessing; see Reboussin et al. 2015; Krijt & Ciesla 2016; Bai 2016; Xu et al. 2017; Francis et al. 2022; Furuya et al. 2022, and references therein).

(ii) In protoplanetary discs and in the ISM, S is depleted into sulphide minerals to an unknown extent (e.g., FeS or FeS<sub>2</sub>) (Kama et al. 2019; Konstantopoulou et al. 2022). However, given that S follows the abundance profiles of our target sample, this element generally is the least depleted after the exclusion of C, N, and O.

**Table 6.** The references for model atoms used in this study (see Section 4.2).

Element	Reference
C	Amarsi et al. (2019)
N	Amarsi et al. (2020a)
O	Amarsi et al. (2018b)
Na	Lind et al. (2011)
Mg	Asplund et al. (2021)
Al	Nordlander & Lind (2017)
Si	Amarsi & Asplund (2017)
S	Amarsi et al. (in prep.)
K	Reggiani et al. (2019)
Ca	Asplund et al. (2021)
Fe	Amarsi et al. (2022)

(iii) S and Ti are  $\alpha$ -elements with multiple spectral features available in optical range and the most different condensation temperature (Sc is more refractory, yet has significantly less optical spectral lines), but these elements share similar nucleosynthetic history so that the intrinsic [S/Ti] ratio is supposed to be close to zero in the absence of depletion (Kobayashi et al. 2020). Additionally, our approach allows for the first time to use NLTE [S/Ti] ratio instead of LTE [Zn/Ti] ratio.

Finally, the turn-off temperature  $T_{\text{turn-off}} < 1000$  K for all transition disc targets (see Fig. 3 and 4). Since the one-piece fits are statistically preferred for each target, and there are only few derived elemental abundances with condensation temperatures  $T_{\text{cond}} < 1000$  K, setting  $T_{\text{turn-off}}$  becomes less trivial. Hence, we define the upper limit of turn-off temperatures in the transition disc sample to be located between S and Zn condensation temperatures ( $T_{\text{turn-off}} = 700$  K).

## 5.3 Comparison with literature depletion profiles

In Appendix E, we provide a detailed comparison of depletion profiles of transition disc targets from the literature and from our homogeneous analysis. The key findings of this comparison are summarised below:

(i) Depletion profiles for RU Cen (#3), EP Lyr (#6), DY Ori (#7), and GZ Nor (#9), previously classified as “plateau” profiles based on LTE abundances (Oomen et al. 2019), become “saturated” profiles when NLTE corrections are applied (as indicated by p-values).

(ii) In previous studies, the onset of depletion, characterised by  $T_{\text{turn-off}}$ , was reported at varying temperatures for our sample, ranging from 800 K for four out of 10 Galactic targets to 1200 K for CT Ori (#1) and AC Her (#4) (Kluska et al. 2022). In contrast, our analysis reveals a consistently minimal  $T_{\text{turn-off}}$  across all transition disc targets ( $T_{\text{turn-off}} = 700$  K).

Overall, the spectral data collected in this study enabled the determination of a more extensive set of elemental abundances compared to those reported in the literature for transition disc targets (see Table 2). The derived elemental abundances are discussed in the context of depletion in Section 6.



## 6 DISCUSSION

In this section, we analyse the obtained results to gain a deep understanding of the conditions and factors driving the depletion process in post-AGB/post-RGB binaries with transition discs. We do this by comparing the chemical depletion parameters in our targets with: i) other observational parameters of our target sample, ii) chemical depletion parameters in transition disc YSOs, and iii) chemical depletion parameters in the interstellar medium (ISM).

### 6.1 Correlation analysis of known parameters in post-AGB/post-RGB binaries

To comprehensively investigate our diverse sample of the most chemically depleted subclass of post-AGB/post-RGB binaries (transition disc targets) we conducted a correlation analysis on a representative selection of observational parameters to address specific questions, including:

- (i) Photometric parameters (IR colours  $H - K$  and  $W_1 - W_3$ , SED luminosity  $L_{\text{SED}}$ , PLC luminosity  $L_{\text{PLC}}$ , dust-to-star luminosity ratio  $L_{\text{IR}}/L_*$ ): to explore potential connections between the current IR excess and depletion efficiency.
- (ii) Orbital parameters (orbital period  $P_{\text{orb}}$ , eccentricity  $e$ ): to explore whether certain orbital parameter configurations are more prone to depletion.
- (iii) Pulsational parameter (fundamental pulsation period  $P_{\text{puls}}$ ): to investigate the impact of pulsations on the depletion profile.
- (iv) Astrometric parameters (coordinates R.A. and Dec.): to study the spatial distribution of transition disc targets.
- (v) Spectroscopic parameters (effective temperature  $T_{\text{eff}}$ , surface gravity  $\log g$ , metallicity  $[\text{Fe}/\text{H}]$ , C/O ratio, initial metallicity  $[\text{M}/\text{H}]_{0,\text{min}}$ ,  $[\text{Zn}/\text{Ti}]$  and  $[\text{S}/\text{Ti}]$  abundance ratios): to analyse the shape and the scale of depletion patterns in our targets.

The resulting correlation matrix is depicted in Fig. 5 (see Appendix F for individual dependence plots). To examine the behaviour of the dependencies, a logarithmic scale was applied to all parameters except for coordinates and eccentricity. In the following discussion, we address families of correlations, ordered from the most expected to the least.

We found several obvious physical correlations and anti-correlations (Spearman’s coefficient  $|\rho| \geq 0.6$ ), including: i) spectroscopic parameters related to depletion, such as  $[\text{Zn}/\text{Ti}]$ ,  $[\text{S}/\text{Ti}]$ ,  $[\text{S}/\text{Ti}]_{\text{NLTE}}$ ,  $[\text{Zn}/\text{Fe}]$ , and  $[\text{Fe}/\text{H}]$ ; ii) orbital and other parameters ( $P_{\text{orb}}$  and  $e$  are known for six and five targets, respectively), and iii) surface gravity  $\log g$ , effective temperature  $T_{\text{eff}}$ , luminosity  $L_*/L_{\odot}$ , and  $\log(\text{C}/\text{O})$  ratio.

The correlation between  $\log L_{\text{IR}}/L_*$  and  $[\text{S}/\text{Ti}]_{\text{NLTE}}$  abundance ratio is rather unexpected. By excluding the edge-on targets AF Crt (#8) and V1504 Sco (#10), and relatively dust-poor target EP Lyr (#6), the correlation between the IR luminosity and the depletion scale becomes even more prominent. However, this correlation is likely caused by the sample bias.

Another notable finding was a strong anti-correlation of the fundamental pulsation period with  $W_1 - W_3$  colour. However, the circumbinary dust around our targets is produced from a previous phase of mass loss rather than pulsations (van

Winckel 2003), so this correlation may be caused by sample bias as well.

Finally, we note that the adopted luminosities (see PLC luminosities in Table 3) infer the post-RGB evolutionary status of ST Pup (#2), AD Aql (#5), AF Crt (#8), and GZ Nor (#9). We found that the surface  $[\text{O}/\text{H}]$  abundance in these four post-RGB binaries generally deviates the most from the corresponding value predicted by the linear fit of the depletion profile. However, the surface  $[\text{O}/\text{H}]$  abundance in post-AGB binaries generally aligns with the corresponding linear fit of the depletion profile (see Fig. 3 and 4). To quantify this deviation, we used a “de-scaled”  $[\text{O}/\text{S}]$  abundance ratio using the following equation:

$$[\text{O}/\text{S}]_{\text{NLTE}}^{\text{descaled}} = \frac{[\text{O}/\text{S}]_{\text{obs}}}{[\text{O}/\text{S}]_{\text{calc}}}, \quad (3)$$

where  $[\text{O}/\text{S}]_{\text{obs}}$  is the observed  $[\text{O}/\text{S}]$  abundance ratio, while  $[\text{O}/\text{S}]_{\text{calc}} = [\text{S}/\text{Ti}] \cdot \frac{T_{\text{cond,O}} - T_{\text{cond,S}}}{T_{\text{cond,S}} - T_{\text{cond,Ti}}}$  is the  $[\text{O}/\text{S}]$  abundance ratio calculated by scaling the corresponding  $[\text{S}/\text{Ti}]$  abundance ratio. In our sample, the values of  $[\text{O}/\text{S}]_{\text{NLTE}}^{\text{descaled}}$  range from  $\sim 0$  (when  $[\text{O}/\text{H}]$  and  $[\text{S}/\text{H}]$  abundances are similar) to 1 (when  $[\text{O}/\text{H}]$  abundance follows the linear depletion trend).

The correlation between “de-scaled” abundance ratio  $[\text{O}/\text{S}]_{\text{NLTE}}^{\text{descaled}}$  and luminosity  $L_*$  is not significant for the whole sample, but it is prominent for the subsample of confirmed transition disc targets (#1–#6; see Fig. F2). This connection may hint at O depletion being higher in post-AGB binaries than in post-RGB binaries (in other words,  $T_{\text{turn-off}}$  is lower for depletion profiles of post-AGB binaries rather than for those of post-RGB binaries). This is consistent with the results from Mohorian et al. (2024), where the average turn-off temperature for two post-RGB binaries SZ Mon and DF Cyg ( $T_{\text{turn-off, post-RGB}} \approx 1300\text{K}$ ) was found to be higher than the average value for the post-AGB binary sample ( $T_{\text{turn-off, post-AGB}} \approx 1100\text{K}$ ; Oomen et al. 2019). Our investigation will be extended in future work, as it is beyond the scope of this study.

### 6.2 Parallels with chemical depletion in young stars hosting transition discs

Transition discs around young T Tauri ( $M_{\text{T Tauri}} < 2 M_{\odot}$ ) and Herbig Ae/Be ( $2 M_{\odot} < M_{\text{Herbig Ae/Be}} < 10 M_{\odot}$ ) stars are similar to post-AGB/post-RGB transition discs in structure and many physical properties, including a broad near-IR excess indicative of hot dust in the disc, Keplerian rotation, dust disc mass, and dust mineralogy (see, e.g., Follette et al. 2017; de Ruyter et al. 2005; Corporaal et al. 2023; Andrych et al. 2023, 2024, and references therein).

Interestingly, similar to post-AGB/post-RGB binaries, a subclass of young T Tauri and Herbig Ae/Be stars hosting transition discs also exhibits photospheric depletion of refractory elements, a phenomenon known as the  $\lambda$  Boo phenomenon (see, e.g., Andrievsky et al. 2002; Jura 2015; Kama et al. 2015; Jermyn & Kama 2018; Murphy et al. 2020). While both young T Tauri and Herbig Ae/Be stars with  $\lambda$  Boo-like depletion and post-AGB/post-RGB binaries show similar photospheric underabundances of refractory elements, the chemical depletion process is significantly more efficient in post-AGB/post-RGB systems (as indicated by volatile-to-refractory abundance ratios). For instance, the young stars

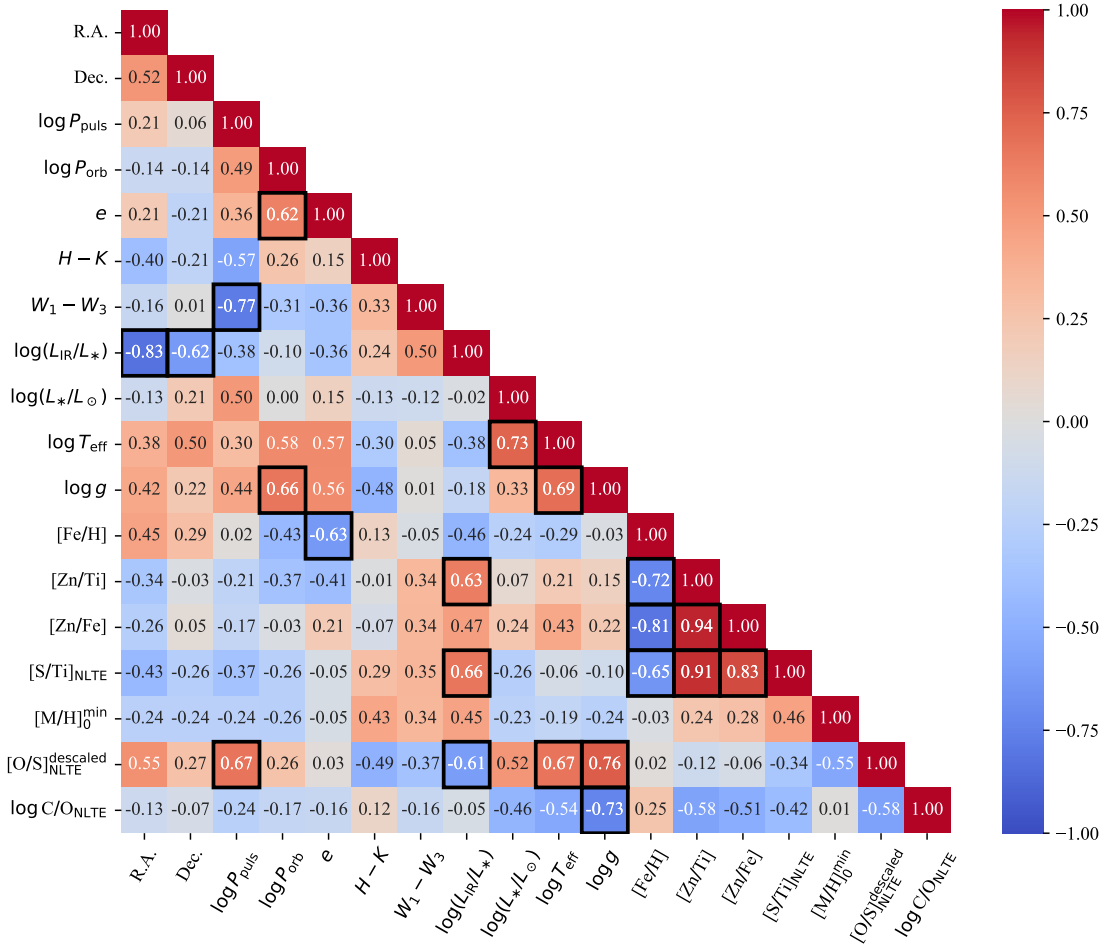


**Figure 5.** Correlation matrix of various stellar parameters of transition disc targets. The strong correlations and anti-correlations (i.e., with Spearman’s correlation coefficients  $|\rho| \geq 0.6$ ) are highlighted with black boxes (for more details, see Section 6.1).

with  $\lambda$  Boo-like depletion show underabundances of Mg, Si, and Fe in the range from 0 to 1 dex (Kama et al. 2015), whereas post-AGB/post-RGB binaries display [Zn/Ti] abundance ratios in the range from 0 to 3.5 dex (Kluska et al. 2022).

In post-AGB/post-RGB binaries, the separation of volatile-rich gas and refractory-rich dust remains poorly understood. In contrast, in young T Tauri and Herbig Ae/Be stars with transition discs and displaying the  $\lambda$  Boo phenomenon, the dust-gas separation is linked to several theoretical mechanisms, including grain growth (Dullemond et al. 2001), photoevaporation (Alexander et al. 2006), dead zones (Regály et al. 2012), and embedded giant planets (Birnstiel, T. et al. 2010). Furthermore, Folsom et al. (2012) suggested that up to a third of Herbig Ae/Be stars hosting protoplanetary discs show signs of depletion and harbour giant planets. Given the structural and chemical parallels between transition discs in  $\lambda$  Boo stars and those in post-AGB/post-RGB binaries, we explore the potential role of giant planets in carving the inner gaps in transition discs around post-AGB/post-RGB binaries.

To study the depletion efficiency in protoplanetary transition discs around young stars, Kama et al. (2015) used the photospheric composition of Herbig Ae/Be single stars as a proxy for the chemical composition of the accreted matter assuming that this matter (with accretion rates of  $\sim 10^{-9} - 10^{-6} M_{\odot}/\text{yr}$ ) quickly dominates the original surface chemistry of a star. Previously, Turcotte (2002) showed that for a young star at an age of  $10^6$  years, the domination of accreted matter may be achieved with the accretion rates of as low as  $\sim 10^{-11} M_{\odot}/\text{yr}$ .

To investigate the depletion efficiency in circumbinary discs around post-AGB/post-RGB stars, Oomen et al. (2019) modelled the accretion rate onto the binary from a viscously evolving disc for a range of accretion rates and disc masses. They showed that to fit the observed parameters, re-accretion in post-AGB/post-RGB stars require significantly larger initial accretion rates than in young stars ( $> 3 \times 10^{-7} M_{\odot}/\text{yr}$ ). Following the approach from Turcotte (2002), we estimate that the re-accreted matter should dominate the original surface material in post-AGB/post-RGB binaries within  $\sim 100$  years. However, this approach is limited by the assumptions

of the negligible impact of binary interaction and the simplified chemical composition of the accreted matter (see Fig. 2 in Oomen et al. 2019).

To compare the depletion scales in our sample and in YSOs, we calculated the depletion strength  $\Delta_{g/d}$  (Kama et al. 2015) given by

$$\Delta_{g/d} = 100 \times 10^{[V/H]-[R/H]} = 100 \times 10^{[V/R]}, \quad (4)$$

where  $[V/H]$  and  $[R/H]$  are the abundances of volatile and refractory tracing elements, respectively. By definition, the solar composition corresponds to depletion strength  $\Delta_{g/d, \odot} = 100$ .

For the  $[V/H]$  and  $[R/H]$  abundances, Kama et al. (2015) combined volatile  $[C/H]$  and  $[O/H]$ , and refractory  $[Fe/H]$ ,  $[Mg/H]$ , and  $[Si/H]$ , respectively. As mentioned in Section 5, we considered volatile  $[S/H]$  and refractory  $[Ti/H]$  to be a more reliable scale of dust depletion. However, for comparison consistency, we used the NLTE-corrected abundances  $[S/H]_{NLTE}$  and  $[Fe/H]_{NLTE}$ , as the depletion tracers in this subsection. Therefore, the expression for the depletion strength  $\Delta_{g/d}$  in transition disc targets is given by

$$\Delta_{g/d} = 100 \times 10^{[S/H]_{NLTE}-[Fe/H]_{NLTE}} = 100 \times 10^{[S/Fe]_{NLTE}}. \quad (5)$$

For young stars hosting transition discs, the depletion strength  $\Delta_{g/d}$  was found to be below  $\approx 10^3$  (see Fig. 2 in Kama et al. 2015). However, for post-AGB/post-RGB targets hosting transition discs, our calculated values of  $\Delta_{g/d}$  lie in the range of higher values (700–20 000; see Table 5). This notable increase of the depletion strength  $\Delta_{g/d}$  in our transition disc targets points at an increased dust depletion efficiency, which may hint at a more effective dust fractionation in the inner circumbinary disc. An alternative explanation could be the dilution efficiency being higher in post-AGB/post-RGB stars due to their smaller atmospheres (van Winckel 2003). However, to solidify our qualitative comparison, there is a clear need to model discs around post-AGB/post-RGB binaries incorporating more sophisticated disc dynamics and more accurate stellar luminosities. Moreover, the assumed chemical composition of the re-accreted matter should be revised taking into account observed patterns, as demonstrated in the present study.

### 6.3 Parallels with chemical depletion in ISM

The ISM is enriched by various sources, including stellar mass-loss, star formation, and supernovae (Zhukovska et al. 2008; Bierbaum et al. 2011; Höfner & Olofsson 2018; Saintonge & Catinella 2022). The gas and dust in the ISM have different chemical compositions, and this difference, known as depletion, is studied by measuring ion column densities in the gas phase (Jenkins 2009). The gas-phase ISM abundances can vary due to factors like differences in star formation, in nucleosynthetic history, or in the condensation of metals into dust grains (De Cia et al. 2016; Konstantopoulou et al. 2022). Distinguishing between these factors, especially at low metallicities, is crucial for studying depletion in the ISM (Jenkins 2014).

A homogeneous research on depletion across various ISM environments, from the Galaxy to damped Ly- $\alpha$  absorbers, was conducted by De Cia et al. (2016). In their study, the ISM sites were distinguished not by the location, but by  $[Zn/Fe]$  abundance ratio: their pointings in the Galaxy and in the

Magellanic Clouds occupied the region of  $[Zn/Fe] > 0.5$  dex, while their pointings towards damped Ly- $\alpha$  absorbers covered the region of  $[Zn/Fe] < 1$  dex. In Fig. 6, the ISM trends of  $[X/Zn]$  abundance ratios for O, S, Mn, Cr, Si, and Mg are denoted with dotted red lines and the corresponding abundance ratios in transition disc targets are shown in black circles and are fitted with black lines. We note that we used NLTE abundances of O, S, and Mg, conditionally NLTE abundances of Cr and Fe (derived from spectral lines of Cr II and Fe II, respectively), and LTE abundances of Mn, Si, and Zn.

We found that the variation in depletion efficiencies of different chemical elements between our transition disc targets and the ISM depends on the volatility of these elements (traced by the corresponding condensation temperatures):

(i) O ( $T_{\text{cond}} = 183$  K; highly volatile): The  $[O/Zn]$  ratio in transition disc targets shows a similar slope as in the ISM (De Cia et al. 2016), but is enhanced by  $\sim 0.4$  dex. However, when compared with the updated trends of the extended ISM sample (see Appendix B2 in Konstantopoulou et al. 2022), the agreement becomes satisfactory.

(ii) S ( $T_{\text{cond}} = 672$  K; moderately volatile): The  $[S/Zn]$  trend in our data is similar to the one observed in the ISM with a slight enhancement by  $\sim 0.2$  dex. However, when distant Ly- $\alpha$  absorbers are excluded (leaving only lines of sight in the Galaxy and the LMC), the agreement becomes satisfactory (see Fig. 1 in Konstantopoulou et al. 2022). We highlight that despite being highly volatile, S may be depleted into dust grains to unknown extent, similarly to interstellar S in the Galaxy (Jenkins 2009) and towards the damped Ly- $\alpha$  absorbers (De Cia et al. 2016).

(iii) Mn ( $T_{\text{cond}} = 1123$  K; moderately volatile): The patterns of  $[Mn/Zn]$  ratios match in our target sample and in the ISM. After accounting for the LTE underabundance of Mn in F and G stars within the solar neighbourhood (Battistini & Bensby 2015), the slope of  $[Mn/Zn]$  vs  $[Fe/Zn]$  approaches unity (see Table 3 in De Cia et al. 2016).

(iv) Cr ( $T_{\text{cond}} = 1291$  K; moderately refractory): The  $[Cr/Zn]$  trends also match in our target sample and in the ISM. The Cr and Fe abundance ratios are identical within the error bars ( $[Cr/Zn] \sim 1.04 \times [Fe/Zn]$ ) in the transition disc targets and in the ISM.

(v) Si ( $T_{\text{cond}} = 1314$  K; moderately refractory): In evolved binaries, the slope of  $[Si/Zn]$  trend is  $-0.64$ , which is lower than the corresponding slope in the ISM. Since Si and Fe have similar condensation temperatures ( $\Delta T_{\text{cond}} = 24$  K) and solar abundances ( $\sim 7.5$  dex), their absolute abundances  $\log \varepsilon(\text{Si})$  and  $\log \varepsilon(\text{Fe})$ <sup>6</sup> in transition disc targets show a 2:3 ratio (Si and Fe abundances in the ISM show a 1:2 ratio; De Cia et al. 2016).

(vi) Mg ( $T_{\text{cond}} = 1343$  K; moderately refractory): The  $[Mg/Zn]$  trend in our targets shows a steeper slope than in the ISM ( $-0.97$  and  $-0.54$ , respectively). Given the close proximity of condensation temperatures ( $\Delta T_{\text{cond}} = 5$  K) and solar abundances of Mg and Fe ( $\sim 7.5$  dex), their absolute abundances  $\log \varepsilon(\text{Mg})$  and  $\log \varepsilon(\text{Fe})$  in transition disc targets show 1:1 abundance ratio.

To summarise, the observed abundance ratios in the tran-

<sup>6</sup> Absolute abundance of an element X is given by:  $\log \varepsilon(X) = \log \frac{N(X)}{N(H)} = [X/H] + \log \varepsilon_{\odot}(X)$ .

sition disc post-AGB/post-RGB targets and in the ISM generally display similar trends for both volatile and refractory elements (O, S, Mn, and Cr). This may be attributed to the fact that all our sample targets are O-rich ( $C/O < 1$ , see Table 5), similar to the O-rich ISM environments studied by De Cia et al. (2016). However, we detected lower slopes in the abundance trends of Si and Mg in the transition disc targets relative to the ISM.

As mentioned above, the  $[X/Zn]$  trends represent both the pure depletion and the nucleosynthetic over- or under-abundance of an element X. To remove the nucleosynthetic effects, De Cia et al. (2016) converted the Galactic abundance patterns from McWilliam (1997) to  $[Zn/Fe]$  scale and provided corrections for the slopes of  $[Cr/Zn]$ ,  $[Si/Zn]$ , and  $[Mg/Zn]$ . Applying these corrections, we obtained  $[Si/Zn]_{\text{corr}} \sim 0.76 \times [Fe/Zn]_{\text{corr}}$ , and  $[Cr/Zn]_{\text{corr}} \sim [Mg/Zn]_{\text{corr}} \sim 1.04 \times [Fe/Zn]_{\text{corr}}$ . Since the solar abundances of Cr and Fe differ by  $\sim 2$  dex, the slope of Cr trend points at independence of the depletion efficiency of an element from its absolute abundance in post-AGB/post-RGB binaries with transition discs. The corrected slopes of Si and Mg trends in post-AGB/post-RGB binaries with transition discs point to Si, Mg, and Fe being depleted in the stellar surface with a number abundance ratio of 0.76:1.04:1, respectively.

Previous studies of circumbinary discs around post-AGB/post-RGB binaries detected Mg-rich end members of olivines (forsterite) and pyroxenes (enstatite) and did not detect Fe-rich dust grains (Gielen et al. 2008, 2009, 2010, 2011; Hillen et al. 2015). Despite this, our measurements of Fe depletion in transition disc targets suggest the existence of Fe grains, such as Fe alloys, Fe oxides, fayalite, or ferrosilite. This highlights the uniqueness of the depletion profile analysis in offering an independent insight into the dust composition in the transition discs around post-AGB/post-RGB binary stars. We note that precise and consistent modelling of infrared spectral features in transition disc targets is beyond the scope of this study, though combining our results with mid-infrared observations from current mid-infrared facilities like MIRI/JWST is a promising avenue for the future research.

## 7 CONCLUSIONS

In this study, we aimed to investigate the mechanisms responsible for depletion, properties of the depletion patterns, and correlations to other observational parameters in post-AGB/post-RGB binary stars with transition discs. In our analysis, we used high-resolution optical spectra from HERMES/Mercator and UVES/VLT.

Using E-iSpec, we performed a detailed chemical abundance analysis of six confirmed transition disc stars and six transition disc candidates in the Galaxy and in the LMC. In addition to the derived LTE abundances, we used **Balder** software to calculate the NLTE corrections for a representative subset of chemical elements from C to Fe. We found that these corrections significantly affect the surface C/O ratios of transition disc targets and modify the depletion patterns. The resulting NLTE-corrected depletion profiles are saturated, meaning that the current surface abundances of all transition disc targets trace the composition of the re-accreted gas, rather than the original photospheric material.

Moreover, we confirmed that depletion efficiency in transition disc systems, as traced by  $[S/Ti]$  abundance ratio, is higher than in other post-AGB/post-RGB binary stars.

In addition, we explored correlations between the derived abundances and various observational parameters associated with the binary system (e.g., astrometric, photometric, orbital, pulsational). For transition disc targets, the detected correlations generally align with those reported in the literature for the broader sample of post-AGB/post-RGB binary stars. Notably, we identified a moderate correlation between stellar luminosity and the normalised  $[O/S]$  abundance ratio. This hints at the turn-off temperature  $T_{\text{turn-off}}$  in transition disc targets being typically lower for depletion profiles in post-AGB binaries than in post-RGB binaries.

We also investigated the links between chemical depletion in our target sample and other environments (around YSOs with transition discs and in the ISM). We confirmed that the homogeneously derived depletion strength ( $\Delta_{g/d, \text{pAGB/pRGB}} = 700 - 20000$ ) in post-AGB/post-RGB binaries with transition discs is significantly higher than the values observed in young stars with transition discs ( $\Delta_{g/d, \text{YSO}} < 1000$ ). However, the depletion patterns in post-AGB/post-RGB binaries with transition discs, as traced by the  $[X/Zn]$  vs.  $[Zn/Fe]$  slopes, resemble those seen in the ISM for both volatile elements (O, S, Mn) and refractory elements (Cr, Fe). We also found that the refractory elements Si and Mg deviate from this trend, indirectly offering a rough estimate of the amount of unobservable Fe dust grains in the transition discs around post-AGB/post-RGB binaries. It is important to note that these findings are based on a limited sample size. Our ongoing analysis of optical spectra of post-AGB/post-RGB binaries in the Galaxy, SMC and LMC aims to expand the target sample to enable a more statistically robust investigation, allowing for further validation and confirmation of current results.

## ACKNOWLEDGEMENTS

The spectroscopic results presented in this paper are based on observations made with the Mercator Telescope, operated on the island of La Palma by the Flemish Community, at the Spanish Observatorio del Roque de los Muchachos of the Instituto de Astrofísica de Canarias. This research is based on observations collected at the European Organisation for Astronomical Research in the Southern Hemisphere under ESO programmes 074.D-0619 and 092.D-0485. This research was supported by computational resources provided by the Australian Government through the National Computational Infrastructure (NCI) under the National Computational Merit Allocation Scheme and the ANU Merit Allocation Scheme (project y89).

MM1 acknowledges the International Macquarie Research Excellence Scholarship (iMQRES) program for the financial support during the research. MM1, DK, and MM2 acknowledge the ARC Centre of Excellence for All Sky Astrophysics in 3 Dimensions (ASTRO 3D), through project CE170100013. AMA acknowledges support from the Swedish Research Council (VR 2020-03940) and from the Crafoord Foundation via the Royal Swedish Academy of Sciences (CR 2024-0015). HVW acknowledges support from the Research Council, KU Leuven under grant number C14/17/082.



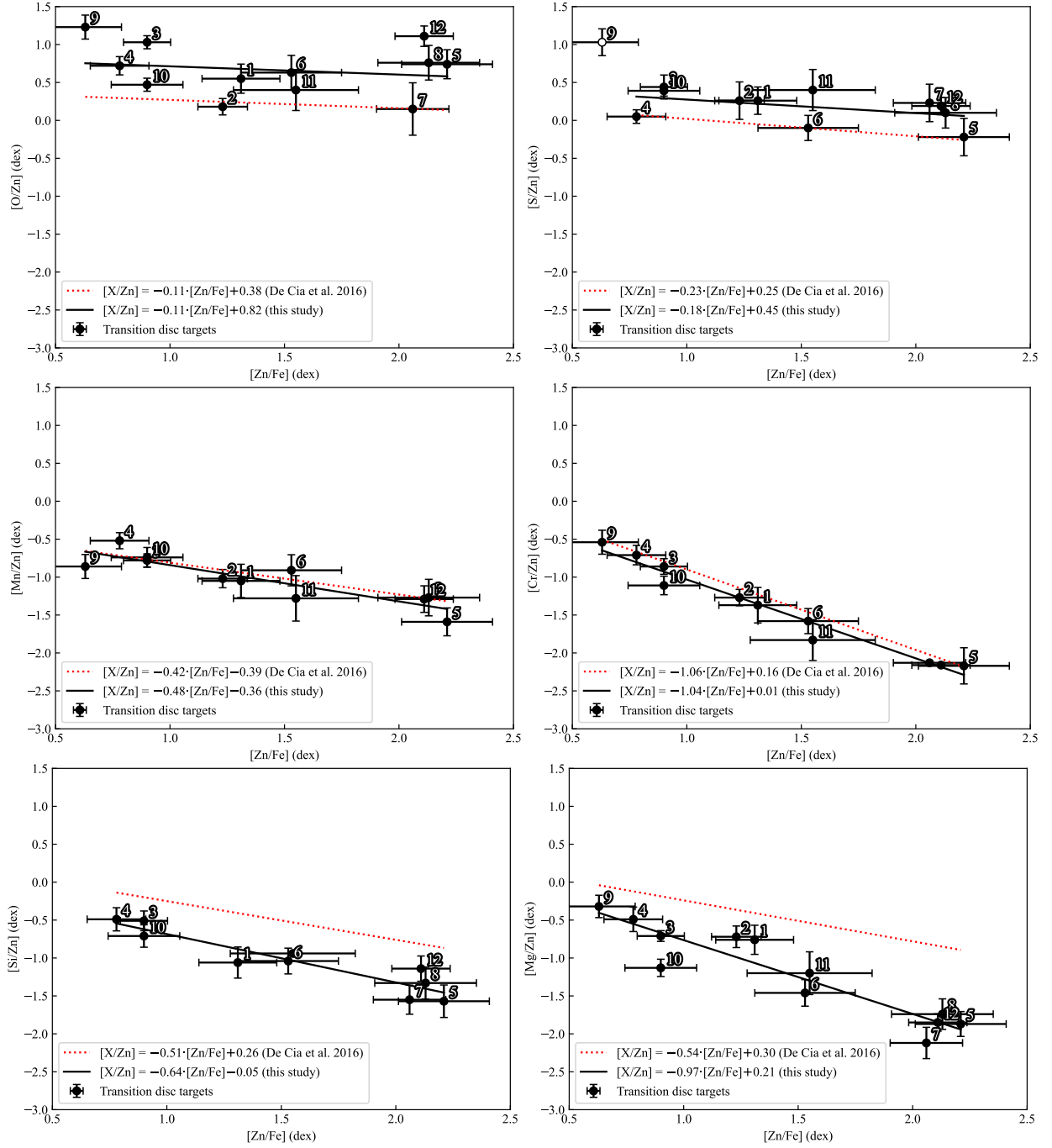


**Figure 6.** Comparison of  $[X/Zn]$  ratio trends for O I, S I, Mn I, Cr I, Si II, and Mg I between transition disc targets and the ISM (De Cia et al. 2016).  $[Zn/Fe]$  was calculated based on abundances from Zn I and Fe II spectral lines. The legend for the symbols and colours used is included within the plot. We note that for  $[S/Zn]$  subplot we excluded GZ Nor (#9) from fitting because of the unique depletion profile of this target (see Fig. 4). We also note that for  $[Cr/Zn]$  ratio of GZ Nor (#9) we used the abundance derived from Cr II lines, while for  $[Si/Zn]$  ratio of LMC V0770 (#11) we used the abundance derived from Si I lines (for more details, see Section 6.3).

## DATA AVAILABILITY

The data underlying this article are available in the article and in its online supplementary material.

## REFERENCES

Alexander R. D., Clarke C. J., Pringle J. E., 2006, *MNRAS*, **369**,

229

- Amarsi A. M., Asplund M., 2017, *MNRAS*, **464**, 264  
 Amarsi A. M., Asplund M., Collet R., Leenaarts J., 2016a, *MNRAS*, **455**, 3735  
 Amarsi A. M., Lind K., Asplund M., Barklem P. S., Collet R., 2016b, *MNRAS*, **463**, 1518  
 Amarsi A. M., Nordlander T., Barklem P. S., Asplund M., Collet R., Lind K., 2018a, *A&A*, **615**, A139  
 Amarsi A. M., Barklem P. S., Asplund M., Collet R., Zatsarinnyy

- O., 2018b, *A&A*, **616**, A89
- Amarsi A. M., Barklem P. S., Collet R., Grevesse N., Asplund M., 2019, *A&A*, **624**, A111
- Amarsi A. M., Grevesse N., Grumer J., Asplund M., Barklem P. S., Collet R., 2020a, *A&A*, **636**, A120
- Amarsi A. M., et al., 2020b, *A&A*, **642**, A62
- Amarsi A. M., Liljegren S., Nissen P. E., 2022, *A&A*, **668**, A68
- Andrievsky S. M., et al., 2002, *A&A*, **396**, 641
- Andrych K., Kamath D., Kluska J., Van Winckel H., Ertel S., Corporaal A., 2023, *MNRAS*, **524**, 4168
- Andrych K., Kamath D., Van Winckel H., Kluska J., Schmid H. M., Corporaal A., Milli J., 2024, *MNRAS*, **535**, 1763
- Asplund M., Amarsi A. M., Grevesse N., 2021, *A&A*, **653**, A141
- Bai X.-N., 2016, *ApJ*, **821**, 80
- Bailer-Jones C. A. L., Rybizki J., Foesneau M., Demleitner M., Andrae R., 2021, *AJ*, **161**, 147
- Battistini C., Bensby T., 2015, *A&A*, **577**, A9
- Bergemann M., Gehren T., 2008, *A&A*, **492**, 823
- Bierbaum V. M., Le Page V., Snow T. P., 2011, in Joblin C., Tielens A. G. G. M., eds, *EAS Publications Series Vol. 46*, EAS Publications Series. pp 427–440, doi:10.1051/eas/1146044
- Birnstiel, T. Dullemond, C. P. Brauer, F. 2010, *A&A*, **513**, A79
- Birnstiel T., Fang M., Johansen A., 2016, *Space Sci. Rev.*, **205**, 41
- Blanco-Cuaresma S., 2019, *MNRAS*, **486**, 2075
- Blanco-Cuaresma S., Soubiran C., Heiter U., Jofré P., 2014, *A&A*, **569**, A111
- Bódi A., Kiss L. L., 2019, *ApJ*, **872**, 60
- Bollen D., Kamath D., Van Winckel H., De Marco O., Verhamme O., Kluska J., Wardle M., 2022, *A&A*, **666**, A40
- Bujarrabal V., Castro-Carrizo A., Alcolea J., Van Winckel H., 2015, *A&A*, **575**, L7
- Bujarrabal V., Castro-Carrizo A., Van Winckel H., Alcolea J., Sánchez Contreras C., Santander-García M., Hillen M., 2018, *A&A*, **614**, A58
- Cardelli J. A., Clayton G. C., Mathis J. S., 1989, *ApJ*, **345**, 245
- Castelli F., Kurucz R. L., 2003, in Piskunov N., Weiss W. W., Gray D. F., eds, *210th Symposium of the International Astronomical Union held at Uppsala University Vol. 210*, Modelling of Stellar Atmospheres. p. A20 (arXiv:astro-ph/0405087)
- Coleman G. A. L., Nelson R. P., Triaud A. H. M. J., 2022, *MNRAS*, **513**, 2563
- Corporaal A., Kluska J., Van Winckel H., Andrych K., Cuello N., Kamath D., Mérand A., 2023, *A&A*, **674**, A151
- Cousins A. W. J., 1976, *Monthly Notes of the Astronomical Society of South Africa*, **35**, 70
- De Cia A., Ledoux O., Mattsson L., Petitjean P., Srianand R., Gagnaud I., Jenkins E. B., 2016, *A&A*, **596**, A97
- De Smedt K., Van Winckel H., Karakas A. I., Siess L., Goriely S., Wood P. R., 2012, *A&A*, **541**, A67
- De Smedt K., Van Winckel H., Kamath D., Karakas A. I., Siess L., Goriely S., Wood P., 2014, *A&A*, **563**, L5
- De Smedt K., Van Winckel H., Kamath D., Wood P. R., 2015, *A&A*, **583**, A56
- De Smedt K., Van Winckel H., Kamath D., Siess L., Goriely S., Karakas A. I., Manick R., 2016, *A&A*, **587**, A6
- Degroote P., Conroy K., Hambleton K., Bloemen S., Pablo H., Giammarco J., Prša A., 2013, in Pavlovski K., Tkachenko A., Torres G., eds, *EAS Publications Series Vol. 64*, EAS Publications Series. pp 277–284, doi:10.1051/eas/1364038
- Dekker H., D’Odorico S., Kaufer A., Delabre B., Kotzłowski H., 2000, in Iye M., Moorwood A. F., eds, *Society of Photo-Optical Instrumentation Engineers (SPIE) Conference Series Vol. 4008*, Optical and IR Telescope Instrumentation and Detectors. pp 534–545, doi:10.1117/12.395512
- Deroo, P. et al., 2006, *A&A*, **450**, 181
- Dullemond C. P., Dominik C., Natta A., 2001, *ApJ*, **560**, 957
- Ertel S., et al., 2019, *AJ*, **157**, 110
- Flower P. J., 1996, *ApJ*, **469**, 355
- Follette K. B., et al., 2017, *AJ*, **153**, 264
- Folsom C. P., Bagnulo S., Wade G. A., Alecian E., Landstreet J. D., Marsden S. C., Waite I. A., 2012, *MNRAS*, **422**, 2072
- Francis L., et al., 2022, *AJ*, **164**, 105
- Furuya K., Lee S., Nomura H., 2022, *ApJ*, **938**, 29
- Gallardo Cava I., 2023, *arXiv e-prints*, p. arXiv:2311.08034
- Gallardo Cava I., Alcolea J., Bujarrabal V., Gómez-Garrido M., Castro-Carrizo A., 2023, *A&A*, **671**, A80
- Gezer I., Van Winckel H., Bozkurt Z., De Smedt K., Kamath D., Hillen M., Manick R., 2015, *MNRAS*, **453**, 133
- Gezer I., Van Winckel H., Manick R., Kamath D., 2019, *MNRAS*, **488**, 4033
- Gielen C., van Winckel H., Min M., Waters L. B. F. M., Lloyd Evans T., 2008, *A&A*, **490**, 725
- Gielen C., et al., 2009, *A&A*, **508**, 1391
- Gielen C., et al., 2010, *A&A*, **515**, C2
- Gielen C., et al., 2011, *A&A*, **533**, A99
- Giridhar S., Lambert D. L., Gonzalez G., 1998, *ApJ*, **509**, 366
- Giridhar S., Lambert D. L., Reddy B. E., Gonzalez G., Yong D., 2005, *ApJ*, **627**, 432
- Gonzalez G., Wallerstein G., 1996, *MNRAS*, **280**, 515
- González-Bolívar M., De Marco O., Bermúdez-Bustamante L. C., Siess L., Price D. J., 2024, *MNRAS*, **527**, 9145
- Gonzalez G., Lambert D. L., Giridhar S., 1997a, *ApJ*, **479**, 427
- Gonzalez G., Lambert D. L., Giridhar S., 1997b, *ApJ*, **481**, 452
- Griffin M. J., et al., 2010, *A&A*, **518**, L3
- Gustafsson B., Edvardsson B., Eriksson K., Jørgensen U. G., Nordlund Å., Plez B., 2008, *A&A*, **486**, 951
- Heath R. M., Nixon C. J., 2020, *A&A*, **641**, A64
- Hillen, M. Kluska, J. Le Bouquin, J.-B. Van Winckel, H. Berger, J.-P. Kamath, D. Bujarrabal, V. 2016, *A&A*, **588**, L1
- Hillen M., de Vries B. L., Menu J., Van Winckel H., Min M., Mulders G. D., 2015, *A&A*, **578**, A40
- Höfner S., Olofsson H., 2018, *A&ARv*, **26**, 1
- Høg E., et al., 2000, *A&A*, **355**, L27
- Ishihara D., et al., 2010, *A&A*, **514**, A1
- Itoh Y., Fukagawa M., Shibai H., Sumi T., Yamamoto K., 2015, *PASJ*, **67**, 88
- Izzard R. G., Jermyn A. S., 2023, *MNRAS*, **521**, 35
- Jenkins E. B., 2009, *ApJ*, **700**, 1299
- Jenkins E. B., 2014, *arXiv e-prints*, p. arXiv:1402.4765
- Jermyn A. S., Kama M., 2018, *MNRAS*, **476**, 4418
- Johnson H. L., Morgan W. W., 1953, *ApJ*, **117**, 313
- Jura M., 2015, *AJ*, **150**, 166
- Kama M., Folsom C. P., Pinilla P., 2015, *A&A*, **582**, L10
- Kama M., Shorttle O., Jermyn A. S., Folsom C. P., Furuya K., Bergin E. A., Walsh C., Keller L., 2019, *ApJ*, **885**, 114
- Kamath D., Van Winckel H., 2019, *MNRAS*, **486**, 3524
- Kamath D., Wood P. R., Van Winckel H., 2014, *MNRAS*, **439**, 2211
- Kamath D., Wood P. R., Van Winckel H., 2015, *MNRAS*, **454**, 1468
- Kamath D., Wood P. R., Van Winckel H., Nie J. D., 2016, *A&A*, **586**, L5
- Kamath D., Dell’Agli F., Ventura P., Van Winckel H., Tosi S., Karakas A. I., 2023, *MNRAS*, **519**, 2169
- Karakas A. I., Lattanzio J. C., 2014, *Publ. Astron. Soc. Australia*, **31**, e030
- Kiss L. L., Deker A., Szabó G. M., Bedding T. R., Szabados L., 2007, *MNRAS*, **375**, 1338
- Kluska J., Van Winckel H., Hillen M., Berger J. P., Kamath D., Le Bouquin J. B., Min M., 2019, *A&A*, **631**, A108
- Kluska J., Van Winckel H., Coppée Q., Oomen G. M., Dsilva K., Kamath D., Bujarrabal V., Min M., 2022, *A&A*, **658**, A36
- Kobayashi C., Karakas A. I., Umeda H., 2011, *MNRAS*, **414**, 3231
- Kobayashi C., Karakas A. I., Lugaro M., 2020, *ApJ*, **900**, 179
- Konstantopoulou C., et al., 2022, *A&A*, **666**, A12
- Krijt S., Ciesla F. J., 2016, *ApJ*, **822**, 111

- Kupka F., Dubernet M. L., VAMDC Collaboration 2011, *Baltic Astronomy*, **20**, 503
- Lagage P. O., Pantin E., 1994, *Nature*, **369**, 628
- Leenaarts J., Carlsson M., 2009, in Lites B., Cheung M., Magara T., Mariska J., Reeves K., eds, *Astronomical Society of the Pacific Conference Series Vol. 415, The Second Hinode Science Meeting: Beyond Discovery-Toward Understanding*. p. 87
- Lind K., Asplund M., Barklem P. S., Belyaev A. K., 2011, *A&A*, **528**, A103
- Lind K., Bergemann M., Asplund M., 2012, *MNRAS*, **427**, 50
- Lodders K., 2003, *ApJ*, **591**, 1220
- Maas T., Van Winckel H., Waelkens C., 2002, *A&A*, **386**, 504
- Maas T., Van Winckel H., Lloyd Evans T., 2005, *A&A*, **429**, 297
- Maas T., Giridhar S., Lambert D. L., 2007, *ApJ*, **666**, 378
- Manick R., Van Winckel H., Kamath D., Sekaran S., Kolenberg K., 2018, *A&A*, **618**, A21
- McWilliam A., 1997, *ARA&A*, **35**, 503
- Menon M., Kamath D., Mohorian M., Van Winckel H., Ventura P., 2024, *Publ. Astron. Soc. Australia*, **41**, e025
- Mészáros S., et al., 2012, *AJ*, **144**, 120
- Mohorian M., Kamath D., Menon M., Ventura P., Van Winckel H., García-Hernández D. A., Masseron T., 2024, *MNRAS*, **530**, 761
- Mösta P., Taam R. E., Duffell P. C., 2019, *ApJ*, **875**, L21
- Muñoz D. J., Miranda R., Lai D., 2019, *ApJ*, **871**, 84
- Murphy S. J., Gray R. O., Corbally C. J., Kuehn C., Bedding T. R., Killam J., 2020, *MNRAS*, **499**, 2701
- Neugebauer G., et al., 1984, *ApJ*, **278**, L1
- Ngeow C.-C., Kanbur S. M., 2005, *MNRAS*, **360**, 1033
- Nordlander T., Lind K., 2017, *A&A*, **607**, A75
- Oomen G.-M., Van Winckel H., Pols O., Nelemans G., Escorza A., Manick R., Kamath D., Waelkens C., 2018, *A&A*, **620**, A85
- Oomen G.-M., Van Winckel H., Pols O., Nelemans G., 2019, *A&A*, **629**, A49
- Oomen G.-M., Pols O., Van Winckel H., Nelemans G., 2020, *A&A*, **642**, A234
- Pawlak M., et al., 2019, *MNRAS*, **487**, 5932
- Penzlin A. B. T., Kley W., Audiffren H., Schäfer C. M., 2022, *A&A*, **660**, A101
- Poglitsch A., et al., 2010, *A&A*, **518**, L2
- Preston G. W., Krzeminski W., Smak J., Williams J. A., 1963, *ApJ*, **137**, 401
- Rao S. S., Giridhar S., 2014, *Rev. Mex. Astron. Astrofis.*, **50**, 49
- Raskin G., et al., 2011, *A&A*, **526**, A69
- Reboussin L., Wakelam V., Guilloteau S., Hersant F., Dutrey A., 2015, *A&A*, **579**, A82
- Regály Z., Juhász A., Sándor Z., Dullemond C. P., 2012, *MNRAS*, **419**, 1701
- Reggiani H., et al., 2019, *A&A*, **627**, A177
- Reyniers M., van Winckel H., 2007, *A&A*, **463**, L1
- Saintonge A., Catinella B., 2022, *ARA&A*, **60**, 319
- Scicluna P., Kemper F., Trejo A., Marshall J. P., Ertel S., Hillen M., 2020, *MNRAS*, **494**, 2925
- Skrutskie M. F., et al., 2006, *AJ*, **131**, 1163
- Snedden C. A., 1973, PhD thesis, University of Texas, Austin
- Stobie R. S., 1970, *MNRAS*, **148**, 1
- Torres G., 2010, *AJ*, **140**, 1158
- Turcotte S., 2002, *ApJ*, **573**, L129
- Van Winckel H., 2018, *arXiv e-prints*, p. [arXiv:1809.00871](https://arxiv.org/abs/1809.00871)
- Van Winckel H., Hrivnak B. J., Gorlova N., Gielen C., Lu W., 2012, *A&A*, **542**, A53
- Ventura P., D'Antona F., Mazzitelli I., 2008, *Ap&SS*, **316**, 93
- Ventura P., Dell'Agli F., Lugaro M., Romano D., Tailo M., Yagüe A., 2020, *A&A*, **641**, A103
- Waelkens C., Van Winckel H., Bogaert E., Trams N. R., 1991, *A&A*, **251**, 495
- Walker S., Butterworth N., Pearce A., 2015, *J. AAVSO*, **43**, 227
- Waters L. B. F. M., Trams N. R., Waelkens C., 1992, *A&A*, **262**, L37
- Wood B. J., Smythe D. J., Harrison T., 2019, *American Mineralogist*, **104**, 844
- Wright E. L., et al., 2010, *AJ*, **140**, 1868
- Xu R., Bai X.-N., Öberg K., 2017, *ApJ*, **835**, 162
- York D. G., et al., 2000, *AJ*, **120**, 1579
- Zagaria F., Rosotti G. P., Alexander R. D., Clarke C. J., 2023, *European Physical Journal Plus*, **138**, 25
- Zhukovska S., Gail H. P., Trieloff M., 2008, *A&A*, **479**, 453
- de Ruyter S., van Winckel H., Dominik C., Waters L. B. F. M., Dejonghe H., 2005, *A&A*, **435**, 161
- de Ruyter S., van Winckel H., Maas T., Lloyd Evans T., Waters L. B. F. M., Dejonghe H., 2006, *A&A*, **448**, 641
- van Aarle E., van Winckel H., Lloyd Evans T., Ueta T., Wood P. R., Ginsburg A. G., 2011, *A&A*, **530**, A90
- van Winckel H., 2003, *ARA&A*, **41**, 391

## APPENDIX A: INDIVIDUAL TARGET DETAILS

In this Appendix, we discuss the previous studies of our target sample, from which we adopted pulsational and orbital parameters, together with luminosity estimates (see Table 2). In Fig. E1, we show the astrometric distribution of transition disc targets.

### A1 Transition disc stars

In this subsection, we present the targets with circumbinary discs, for which the reported dust inner rims  $R_{in}$  are at least 2.5 times larger than the expected dust sublimation radius  $R_{sub}$  (Corporaal et al. 2023). The presence of large, dust-free cavities in the discs around CT Ori, ST Pup, RU Cen, AC Her, AD Aql, and EP Lyr indicates these systems have transition discs, similar to those found around YSOs.

#### A1.1 CT Ori (#1)

CT Ori, characterised as an RV Tau variable (spectroscopic class B<sup>7</sup>), exhibits a fundamental<sup>8</sup> pulsation period of 33.65 days with no RVb phenomenon (slow variation in mean magnitude with a long secondary period  $P \sim 600 - 2600$  days), as observed by Kiss et al. (2007). The orbital parameters of CT Ori are not constrained yet. Based on SED fitting, the luminosity of CT Ori was estimated to be  $L_{SED} = 15100L_{\odot}$  by Oomen et al. (2019). Kluska et al. (2022) obtained a disc-star luminosity ratio for CT Ori  $L_{IR}/L_{*} = 0.55$ . Corporaal et al. (2023) confirmed the transition disc nature of CT Ori with  $R_{in}/R_{sub} \sim 4.5$ . Gonzalez et al. (1997b) conducted a comprehensive abundance analysis of CT Ori and identified significant depletion with  $[Fe/H] = -2.0$  dex and  $[Zn/Ti] = 1.9$  dex.

<sup>7</sup> RV Tau variables of spectroscopic classes A, B, and C are metal-rich, metal-poor with enhanced carbon, and metal-poor without carbon enhancement, respectively (Preston et al. 1963).

<sup>8</sup> The fundamental pulsation period for Type II Cepheids is twice shorter than the double period which usually is the best-fit value for phase-folded light curves (Stobie 1970).

### A1.2 ST Pup (#2)

ST Pup is classified as a W Vir pulsating variable. Walker et al. (2015) has determined the fundamental pulsation period of ST Pup (18.73 days). Despite the absence of the RVb phenomenon, Oomen et al. (2018) calculated the orbital parameters of ST Pup using data from the long-term radial-velocity monitoring campaign ( $P_{\text{orb}} = 406 \pm 2$  d,  $e = 0.00 \pm 0.04$ ). Oomen et al. (2019) reported the luminosity estimate for ST Pup through SED fitting ( $L_{\text{SED}} = 690 L_{\odot}$ ). Kluska et al. (2022) obtained a moderate disc-star luminosity ratio of  $L_{\text{IR}}/L_{*} = 0.72$ . According to Corporaal et al. (2023), the ratio of dust inner rim to dust sublimation radius for ST Pup is  $R_{\text{in}}/R_{\text{sub}} \sim 3$ . Gonzalez & Wallerstein (1996) analysed the chemical composition of ST Pup, revealing significant depletion ( $[\text{Fe}/\text{H}] = -1.5$  dex,  $[\text{Zn}/\text{Ti}] = 2.1$  dex).

### A1.3 RU Cen (#3)

RU Cen, classified as an RV Tau variable (spectroscopic class B), has a fundamental pulsation period of 32.37 days, as documented by Bódi & Kiss (2019) (RVb phenomenon was not detected). By using radial velocities from various spectral observations, Oomen et al. (2018) determined the orbital parameters of RU Cen to be  $P_{\text{orb}} = 1489 \pm 10$  days and  $e = 0.62 \pm 0.07$ . The luminosity of RU Cen was estimated to be  $L_{\text{SED}} = 1100 L_{\odot}$  based on SED fitting by Oomen et al. (2019). Kluska et al. (2022) provided a moderate disc-star luminosity ratio of  $L_{\text{IR}}/L_{*} = 0.40$ . Corporaal et al. (2023) reported  $R_{\text{in}}/R_{\text{sub}} \sim 3.5$  for RU Cen. Maas et al. (2002) conducted a detailed abundance analysis of RU Cen and reported significant depletion with  $[\text{Fe}/\text{H}] = -1.9$  dex and  $[\text{Zn}/\text{Ti}] = 1.0$  dex.

### A1.4 AC Her (#4)

AC Her, an RV Tau pulsating variable of spectroscopic class B, has a fundamental pulsation period of 37.73 days as determined by Giridhar et al. (1998). There is no apparent RVb phenomenon in this star. Using radial velocities from long-term spectral observations, Oomen et al. (2018) derived the orbital parameters of AC Her ( $P_{\text{orb}} = 1189 \pm 1$  days and  $e = 0.0 \pm 0.05$ ). The luminosity of AC Her was estimated to be  $L_{\text{SED}} = 2400 L_{\odot}$  based on SED fitting by Oomen et al. (2019). Bollen et al. (2022) modelled jets in this system and obtained an independent estimate of luminosity for this target  $L_{\text{jet model}} = 3600 L_{\odot}$ . Kluska et al. (2022) reported a low disc-star luminosity ratio  $L_{\text{IR}}/L_{*} = 0.21$ . In the study by Corporaal et al. (2023), the ratio of inner rim to sublimation radius for AC Her was found to be  $R_{\text{in}}/R_{\text{sub}} \sim 7.5$ . Giridhar et al. (1998) performed a detailed abundance analysis of AC Her and found moderate depletion with  $[\text{Fe}/\text{H}] = -1.4$  dex and  $[\text{Zn}/\text{Ti}] = 0.7$  dex.

### A1.5 AD Aql (#5)

AD Aql, classified as an RV Tau variable (spectroscopic class B), has a fundamental pulsation period of 32.7 days, as documented by Giridhar et al. (1998) (RVb phenomenon was not detected for this target). The orbital parameters of AD Aql are not studied yet. The luminosity of AD Aql was estimated to be  $L_{\text{SED}} = 11500 L_{\odot}$  based on SED fitting by Oomen

et al. (2019). Kluska et al. (2022) obtained a rather moderate disc-star luminosity ratio of  $L_{\text{IR}}/L_{*} = 0.51$ . Corporaal et al. (2023) reported  $R_{\text{in}}/R_{\text{sub}} \sim 6$  for AD Aql. Giridhar et al. (1998) analysed the chemical composition of AD Aql and reported high depletion with  $[\text{Fe}/\text{H}] = -2.1$  dex and  $[\text{Zn}/\text{Ti}] = 2.5$  dex.

### A1.6 EP Lyr (#6)

EP Lyr is an RV Tau pulsating variable of spectroscopic class B. This target possesses a fundamental pulsation period of 41.59 days (Bódi & Kiss 2019) with no evident long-period variation. Oomen et al. (2018) employed radial velocities from long-term radial-velocity monitoring campaign to derive the orbital parameters of EP Lyr ( $P_{\text{orb}} = 1151 \pm 14$  days and  $e = 0.39 \pm 0.09$ ). Oomen et al. (2019) estimated the luminosity of EP Lyr through SED fitting ( $L_{\text{SED}} = 5500 L_{\odot}$ ). Furthermore, Bollen et al. (2022) modelled jets in this system and obtained an independent estimate of luminosity for EP Lyr  $L_{\text{jet model}} = 7100 L_{\odot}$ . The disc-star luminosity ratio of  $L_{\text{IR}}/L_{*} = 0.02$  (Kluska et al. 2022) is the lowest in the target sample. Corporaal et al. (2023) derived the ratio of inner rim to sublimation radius  $R_{\text{in}}/R_{\text{sub}} \sim 3.5$  for EP Lyr. Gonzalez et al. (1997a) performed a detailed abundance analysis of EP Lyr, revealing moderate depletion with  $[\text{Fe}/\text{H}] = -1.8$  dex and  $[\text{Zn}/\text{Ti}] = 1.3$  dex.

## A2 Transition disc candidates

In this subsection, we present the targets classified by Kluska et al. (2022) as category 2 ( $W_1 - W_3 > 4.5$ ) and category 3 ( $2.3 < W_1 - W_3 < 4.5$ ,  $H - K < 0.3$ ). Even though category 3 of colour-colour plot is populated by both full disc and transition disc candidates (Kluska et al. 2022), these subclasses may be distinguished by the depletion scale:  $[\text{Zn}/\text{Ti}]_{\text{full-disc}} \sim 0$  dex,  $[\text{Zn}/\text{Ti}]_{\text{transition-disc}} > 0.7$  dex.

### A2.1 DY Ori (#7)

DY Ori is an RV Tau pulsator of spectroscopic class B. ASAS (Pawlak et al. 2019) provides the fundamental pulsation period of DY Ori (30.155 days) with no obvious RVb phenomenon. However, Oomen et al. (2018) used radial velocities of multiple spectral observations of DY Ori to derive the orbital parameters of this target ( $P_{\text{orb}} = 1248 \pm 36$  d,  $e = 0.22 \pm 0.08$ ). Oomen et al. (2019) estimated the luminosity of DY Ori based on the SED fitting ( $L_{\text{SED}} = 21500 L_{\odot}$ ). Kluska et al. (2022) reported a moderate disc-star luminosity ratio  $L_{\text{IR}}/L_{*} = 0.55$ . Gonzalez et al. (1997a) conducted a detailed abundance analysis of DY Ori and detected high depletion with  $[\text{Fe}/\text{H}] = -2.0$  dex and  $[\text{Zn}/\text{Ti}] = 2.1$  dex.

### A2.2 AF Crt (#8)

AF Crt, a W Vir pulsator, has a double pulsation period of 31.5 days as determined by Kiss et al. (2007) without any apparent variation in mean magnitude on the order of hundreds of days. The orbital parameters of AF Crt are not constrained yet. The luminosity of AF Crt was estimated to be  $L_{\text{SED}} = 280 L_{\odot}$  based on SED fitting by Oomen et al. (2019). Kluska et al. (2022) derived a rather high disc-star



luminosity ratio  $L_{\text{IR}}/L_* = 1.83$ . [Van Winckel et al. \(2012\)](#) performed a detailed abundance analysis of AF Crt and reported high depletion of this target with  $[\text{Fe}/\text{H}] = -2.7$  dex and  $[\text{Zn}/\text{Sc}] = 3.4$  dex (a slightly less refractory Sc was used for volatile-to-refractory ratio, since Ti abundance was not calculated).

### A2.3 GZ Nor (#9)

GZ Nor, classified as an RV Tau pulsator, demonstrates a fundamental pulsation period of 36.2 days ([Gezer et al. 2019](#)). No evident RVb phenomenon was observed and no orbital parameters were derived for GZ Nor. [Oomen et al. \(2019\)](#) determined the luminosity of GZ Nor through SED fitting  $L_{\text{SED}} = 1400 L_{\odot}$ . [Kluska et al. \(2022\)](#) provided a mild disc-star luminosity ratio of  $L_{\text{IR}}/L_* = 0.22$ . [Gezer et al. \(2019\)](#) studied the chemical composition of GZ Nor and detected moderate depletion with  $[\text{Fe}/\text{H}] = -2.1$  dex and  $[\text{Zn}/\text{Ti}] = 0.8$  dex.

### A2.4 V1504 Sco (#10)

V1504 Sco is an RV Tau variable star of spectroscopic class B. [Kiss et al. \(2007\)](#) provided the fundamental pulsation period of this star (22.0 d) with a detected RVb phenomenon. Studying the mean magnitude variation, [Kiss et al. \(2007\)](#) derived the orbital period of V1504 Sco ( $P_{\text{orb}} = 735 \pm 230$  d). [Oomen et al. \(2019\)](#) estimated the luminosity of V1504 Sco based on the SED fitting ( $L_{\text{SED}} = 1100 L_{\odot}$ ). [Kluska et al. \(2022\)](#) reported an extreme disc-star luminosity ratio  $L_{\text{IR}}/L_* = 4.69$ . [Maas et al. \(2005\)](#) conducted a detailed abundance analysis of V1504 Sco and detected high depletion with  $[\text{Fe}/\text{H}] = -1.0$  dex and  $[\text{Zn}/\text{Ti}] = 1.4$  dex.

### A2.5 LMC V0770 (#11)

LMC V0770, an RV Tau pulsator, exhibits a fundamental pulsation period of 31.2 days, as determined by [Manick et al. \(2018\)](#). No variation in the mean magnitude was detected and no orbital parameters were constrained for LMC V0770. [Oomen et al. \(2019\)](#) used SED fitting to calculate the luminosity of LMC V0770 ( $L_{\text{SED}} = 3300 L_{\odot}$ ). Moreover, [Manick et al. \(2018\)](#) used PLC relation to obtain an independent estimate of luminosity ( $L_{\text{PLC}} = 2629 L_{\odot}$ ). According to [Kluska et al. \(2022\)](#), the disc-star luminosity ratio for LMC V0770 is moderate  $L_{\text{IR}}/L_* = 0.63$ . [Kamath & Van Winckel \(2019\)](#) analysed the chemical composition of LMC V0770 and reported a high depletion with  $[\text{Fe}/\text{H}] = -2.6$  dex and  $[\text{Zn}/\text{Ti}] = 2.3$  dex.

### A2.6 LMC V3156 (#12)

LMC V3156, an RV Tau pulsator, has a fundamental pulsation period of 46.7 days, as provided by [Manick et al. \(2018\)](#). There is no apparent RVb phenomenon in the light curves of this target and no known orbital parameters. The luminosity of LMC V3156 was estimated by [Manick et al. \(2018\)](#) using two methods: SED fitting and PLC relation ( $L_{\text{SED}} = 5900 L_{\odot}$ ,  $L_{\text{PLC}} = 6989 L_{\odot}$ ). [van Aarle et al. \(2011\)](#) reported a disc-star luminosity ratio of  $L_{\text{IR}}/L_* = 0.84$ .

[Reyniers & van Winckel \(2007\)](#) conducted a detailed abundance analysis of LMC V3156 and found significantly high depletion with  $[\text{Fe}/\text{H}] = -2.4$  dex and  $[\text{Zn}/\text{Ti}] = 2.5$  dex.

## APPENDIX B: SED PLOTS OF THE TARGET SAMPLE

In Table B1, we present the photometric data collected for SED plots of the target sample. In Fig. B1 and B2, we provide our SED plots for all transition disc stars and candidates, respectively (see Section 3.1).

## APPENDIX C: SUMMARY OF OPTICAL SPECTRAL VISITS

In Table C1, we list all optical spectral visits considered in this work (HERMES and UVES; see Section 3.3) for our chemical analysis of the target sample (see Section 4).

## APPENDIX D: MASTER LINE LIST OF THE TARGET SAMPLE

In Table D1, we provide the combined optical line list, which we used to derive the atmospheric parameters and elemental abundances of all 12 transition disc targets (see Section 4).

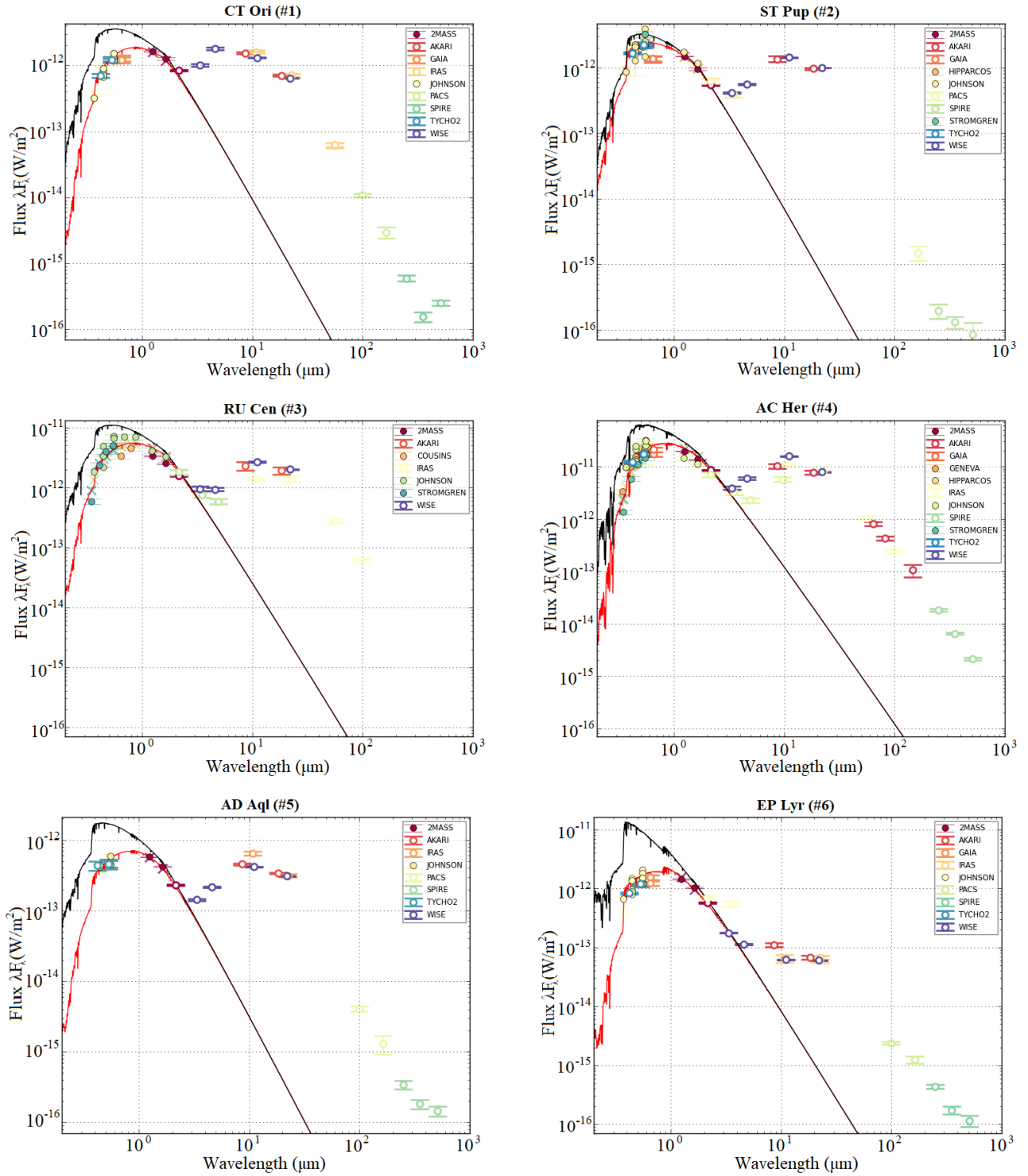


**Figure B1.** Spectral energy distribution of transition disc stars. The red solid line is the appropriate reddened Kurucz model atmosphere. The black solid line is the de-reddened model scaled to the object. We note that the photometric observations of our sample were obtained with different surveys at different time (pulsation phases). We also note that the IR dust excess in SED plots for AF Crt (#8) and V1504 Sco (#10) imply that we see these two targets edge-on. The legend for the symbols and colours used is included within the plot.

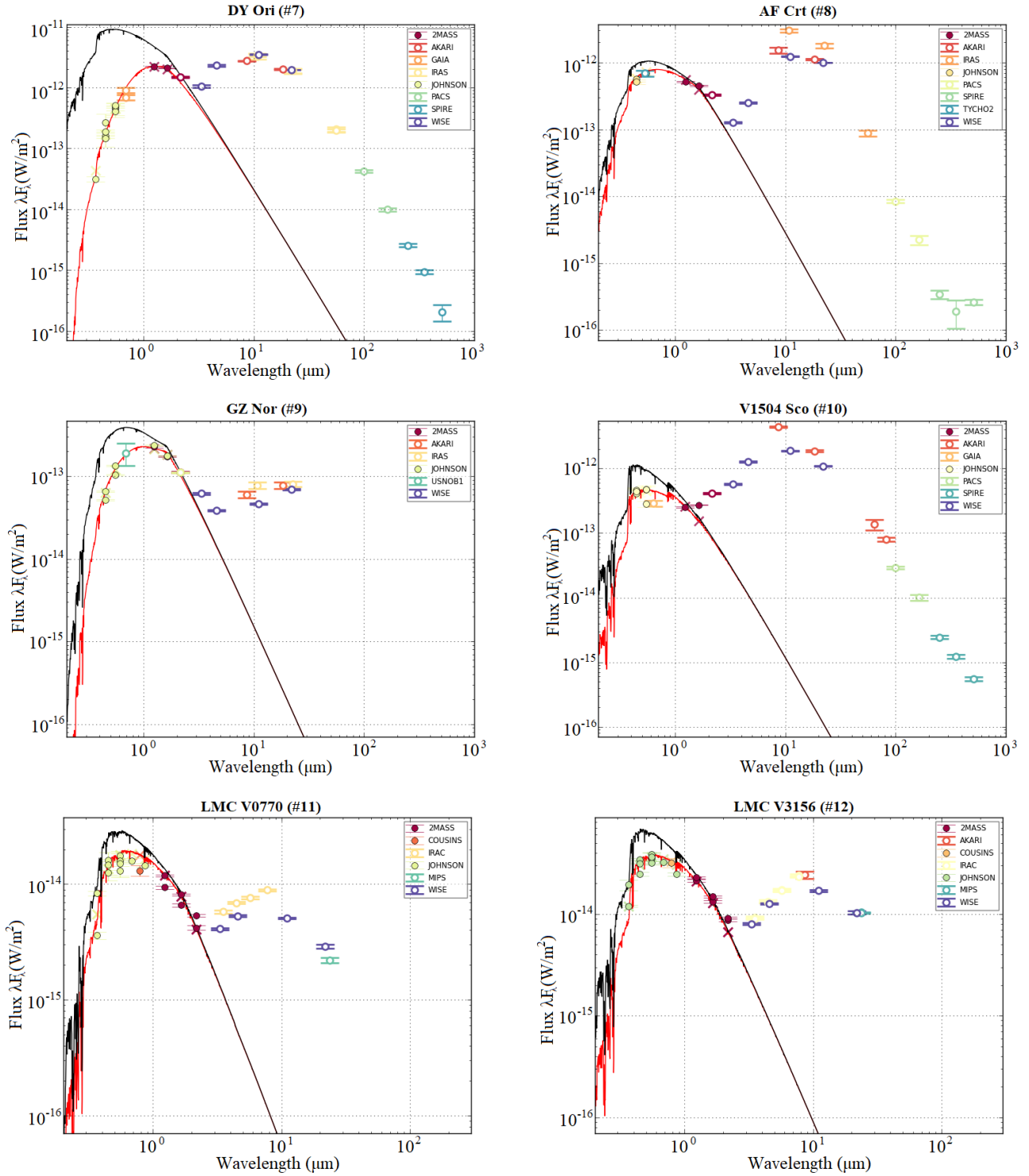


**Figure B2.** Spectral energy distribution of transition disc candidates. The red solid line is the appropriate reddened Kurucz model atmosphere. The black solid line is the de-reddened model scaled to the object. We note that the photometric observations of our sample were obtained with different surveys at different time (pulsation phases). We also note that the IR dust excess in SED plots for AF Crt (#8) and V1504 Sco (#10) imply that we see these two targets edge-on. The legend for the symbols and colours used is included within the plot.

**Table B1.** Photometric data for the target sample (see Section 3.1). For each filter we provide the units and the central wavelengths in  $\mu\text{m}$ . This table is published in its entirety in the electronic edition of the paper. A portion is shown here for guidance regarding its form and content.

ID	Name	GENEVA.U (GCPD)	STROMGREN.U (II/215/catalog)	...	SPIRE.350 (SPIRE350)	SPIRE.500 (SPIRE500)
		mag 0.342	mag 0.346	...	Jy 348.438	Jy 500.412
1	CT Ori	–	–	...	0.018±0.003	0.042±0.004
2	ST Pup	–	–	...	0.015±0.003	0.014±0.007
3	RU Cen	–	12.105±99.999	...	–	–
4	AC Her	9.419±0.116	11.203±99.999	...	0.75±0.04	0.35±0.02
5	AD Aql	–	–	...	0.021±0.003	0.024±0.004
6	EP Lyr	–	–	...	0.020±0.003	0.019±0.004
...	...	...	...	...	...	...

**Note:** We list uncertainties which are unavailable as ‘99.999’.

**Table C1.** All spectral visits of the target sample. This table is published in its entirety in the electronic edition of the paper. A portion is shown here for guidance regarding its form and content.

Visit	MJD	Phase	RV	eRV	SNR
CT Ori (#1) (127 visits)					
00273152	55221.91376	0.00	62.60	0.63	26.38
00314017	55500.22492	0.40	60.29	0.64	24.22
00314465	55507.12069	0.61	53.92	0.97	27.18
00325348	55553.04197	0.99	60.79	0.55	23.79
00327525	55576.97777	0.72	51.61	1.18	22.50
...					



**Table D1.** Combined optical line list of our sample. This table is published in its entirety in the electronic edition of the paper. A portion is shown here for guidance regarding its form and content.

Element	Atomic data			$W_\lambda$ (mÅ)											
	$\lambda$ (nm)	$\log gf$ (dex)	$\chi$ (eV)	CT Ori (#1)	ST Pup (#2)	RU Cen (#3)	AC Her (#4)	AD Aql (#5)	EP Lyr (#6)	DY Ori (#7)	AF Crt (#8)	GZ Nor (#9)	V1504 Sco (#10)	LMC V0770 (#11)	LMC V3156 (#12)
C I	477.1730	-1.866	7.488	-	-	82.6	-	-	-	-	-	-	64.6	-	-
C I	493.2049	-1.658	7.685	123.6	56.7	89.8	62.8	109.0	68.0	86.5	-	-	-	72.3	66.3
C I	502.3841	-2.210	7.946	-	-	-	-	-	-	-	-	-	-	26.4	-
C I	503.9057	-1.790	7.946	-	-	-	-	-	-	-	-	-	-	63.8	33.7
C I	505.2144	-1.303	7.685	-	94.3	123.0	-	-	-	134.1	124.5	92.0	-	-	90.4
C I	538.0325	-1.616	7.685	120.0	52.8	98.6	-	-	68.3	83.8	-	57.6	-	81.4	57.0
								...							

**APPENDIX E: INDIVIDUAL DEPLETION PROFILES**

In Table E1, we provide all elemental abundances derived in this study (see Section 4.1). In Table E2, we provide the atmospheric parameters and differential NLTE corrections for transition disc targets (see Section 4.2). In Fig. E1, we present the spatial distribution of transition disc targets.

**Table E1.** 1D LTE and 1D NLTE elemental abundances of transition disc targets in [X/H] scale.

Ion	$T_{\text{cond}}$	CT Ori (#1)	ST Pup (#2)	RU Cen (#3)	AC Her (#4)	AD Aql (#5)	EP Lyr (#6)	DY Ori (#7)	AF Crt (#8)	GZ Nor (#9)	V1504 Sco (#10)	LMC V0770 (#11)	LMC V3156 (#12)
LTE													
C I	40	-0.57±0.09	-0.50±0.07	-0.44±0.07	-0.59±0.06	-0.10±0.13	-0.28±0.07	0.16±0.08	-0.41±0.09	0.32±0.02	-0.11±0.07	-0.75±0.02	-0.34±0.09
N I	123	-0.78±0.18	-	0.13±0.11	-0.03±0.11	-0.03±0.21	0.07±0.14	0.38±0.19	-0.54±0.19	0.84±0.10	0.59±0.13	-	-
O I	183	0.03±0.09	-0.50±0.05	-0.01±0.12	0.01±0.08	0.75±0.17	0.14±0.14	0.32±0.17	0.43±0.17	0.50±0.06	0.31±0.11	-0.40±0.10	0.78±0.14
Na I	1035	-0.33±0.06	-0.62±0.05	-0.92±0.05	-0.55±0.11	-0.40±0.05	-1.07±0.14	0.32±0.15	0.24±0.17	-1.51±0.10	0.48±0.11	-0.70±0.10	0.47±0.14
Mg I	1343	-1.36±0.10	-1.45±0.08	-1.68±0.08	-1.20±0.07	-1.88±0.10	-1.91±0.08	-1.99±0.12	-2.03±0.12	-1.65±0.03	-1.21±0.09	-2.15±0.07	-2.21±0.12
Al I	1652	-2.40±0.16	-	-	-1.86±0.13	-	-	-	-2.81±0.16	-	-	-3.83±0.10	-2.64±0.15
Si I	1314	-	-	-1.48±0.10	-1.18±0.03	-	-1.66±0.12	-	-	-	-0.75±0.10	-1.99±0.10	-
Si II	1314	-1.63±0.14	-	-1.55±0.12	-1.20±0.13	-1.56±0.17	-1.52±0.08	-1.47±0.14	-1.66±0.11	-	-0.87±0.13	-	-1.47±0.14
S I	672	-0.17±0.06	-0.34±0.10	-0.42±0.08	-0.49±0.03	0.03±0.12	-0.38±0.04	0.62±0.08	-0.07±0.07	-0.12±0.06	0.41±0.10	-0.36±0.01	0.07±0.08
K I	993	-0.47±0.15	-	-0.74±0.12	-0.55±0.07	-0.09±0.17	-1.41±0.14	-	-0.81±0.15	-1.31±0.10	-	-	0.34±0.15
Ca I	1535	-1.64±0.11	-2.04±0.06	-1.86±0.05	-1.45±0.07	-2.43±0.08	-2.02±0.11	-1.76±0.14	-2.22±0.11	-1.92±0.03	-1.41±0.06	-2.56±0.10	-1.79±0.12
Ca II	1535	-1.81±0.14	-	-	-1.57±0.13	-2.64±0.16	-	-2.04±0.13	-2.23±0.15	-	-	-	-
Sc II	1541	-2.55±0.10	-2.48±0.05	-2.09±0.08	-1.96±0.07	-	-2.29±0.11	-	-	-2.15±0.10	-1.63±0.06	-3.74±0.09	-2.64±0.10
Ti I	1565	-	-2.53±0.13	-1.92±0.06	-1.64±0.10	-	-	-	-	-	-	-	-
Ti II	1565	-2.48±0.11	-2.44±0.04	-1.99±0.07	-1.85±0.07	-3.32±0.12	-2.20±0.10	-1.77±0.14	-3.45±0.15	-1.94±0.03	-1.81±0.07	-3.40±0.06	-2.95±0.09
V II	1370	-	-1.79±0.02	-1.81±0.11	-1.38±0.06	-	-1.74±0.13	-	-	-1.78±0.01	-1.56±0.11	-	-1.94±0.13
Cr I	1291	-1.86±0.13	-2.19±0.07	-1.97±0.06	-1.45±0.07	-2.22±0.10	-2.19±0.17	-2.05±0.16	-	-	-1.24±0.08	-2.79±0.09	-2.49±0.14
Cr II	1291	-1.94±0.11	-1.95±0.03	-1.90±0.06	-1.42±0.07	-2.16±0.16	-2.06±0.07	-	-	-1.80±0.04	-1.27±0.07	-2.77±0.00	-
Mn I	1123	-1.62±0.13	-1.70±0.06	-1.82±0.05	-1.23±0.07	-1.58±0.16	-1.39±0.14	-	-1.60±0.16	-2.12±0.05	-0.90±0.09	-2.22±0.05	-1.62±0.12
Mn II	1123	-	-1.74±0.10	-	-	-	-1.35±0.13	-	-	-	-	-2.20±0.10	-
Fe I	1338	-1.85±0.11	-1.91±0.06	-1.93±0.05	-1.47±0.06	-2.24±0.10	-1.98±0.10	-1.97±0.12	-2.46±0.15	-1.90±0.03	-1.06±0.07	-2.61±0.03	-2.47±0.11
Fe II	1338	-1.89±0.07	-1.92±0.03	-1.95±0.07	-1.48±0.07	-2.21±0.14	-2.02±0.08	-1.98±0.08	-2.49±0.11	-1.89±0.04	-1.03±0.07	-2.50±0.02	-2.48±0.09
Co I	1354	-	-1.85±0.13	-1.84±0.12	-1.45±0.13	-2.00±0.14	-1.91±0.16	-	-	-1.42±0.11	-0.84±0.14	-2.55±0.10	-
Ni I	1363	-1.37±0.16	-1.92±0.05	-1.77±0.04	-1.33±0.06	-2.14±0.14	-2.09±0.15	-1.84±0.15	-	-1.62±0.06	-1.13±0.12	-3.05±0.12	-2.00±0.17
Cu I	1034	-1.10±0.17	-1.46±0.09	-	-	-	-	0.42±0.16	-1.13±0.18	-	-	-	-0.08±0.15
Zn I	704	-0.57±0.12	-0.68±0.06	-1.04±0.04	-0.71±0.06	0.01±0.11	-0.48±0.12	0.08±0.13	-0.33±0.13	-1.26±0.08	-0.16±0.07	-0.94±0.19	-0.33±0.09
Sr II	1548	-	-	-	-	-	-	-	-2.51±0.19	-1.54±0.10	-	-2.84±0.10	-
Y II	1551	-2.45±0.13	-2.75±0.05	-2.22±0.11	-1.95±0.10	-	-2.29±0.14	-1.64±0.14	-	-2.23±0.10	-1.58±0.07	-	-2.91±0.14
Zr II	1722	-	-2.89±0.11	-2.15±0.12	-	-	-	-	-	-2.05±0.10	-	-	-
Ba II	1423	-1.92±0.15	-2.15±0.12	-2.01±0.08	-1.52±0.09	-2.53±0.16	-2.14±0.16	-1.97±0.13	-2.92±0.17	-	-1.16±0.13	-3.56±0.10	-1.93±0.13
La II	1615	-	-2.56±0.05	-	-	-	-	-	-	-2.07±0.04	-	-	-
Ce II	1454	-	-2.18±0.11	-1.79±0.12	-1.41±0.07	-	-	-	-	-	-2.01±0.04	-	-
Nd II	1630	-	-	-	-	-	-	-	-	-1.97±0.05	-	-	-
Sm II	1545	-	-	-	-	-	-	-	-	-1.91±0.10	-	-	-
Eu II	1491	-	-1.71±0.11	-	-	-	-	-	-	-	-	-	-
NLTE													
C I	40	-0.70±0.09	-0.61±0.07	-0.57±0.07	-0.69±0.06	-0.24±0.13	-0.41±0.07	-0.07±0.08	-0.55±0.09	0.09±0.04	-0.26±0.06	-0.87±0.01	-0.52±0.09
N I	123	-0.89±0.18	-	-0.01±0.10	-0.16±0.10	-0.17±0.21	-0.12±0.15	0.08±0.19	-0.80±0.19	0.70±0.10	0.39±0.13	-	-
O I	183	-0.02±0.09	-0.5±0.05	-0.01±0.12	0.01±0.08	0.75±0.17	0.15±0.14	0.23±0.23	0.43±0.17	-0.03±0.06	0.31±0.11	-0.54±0.10	0.78±0.14
Na I	1035	-0.49±0.06	-0.74±0.05	-1.03±0.06	-0.70±0.11	-0.55±0.05	-1.45±0.14	0.07±0.12	-0.53±0.17	-1.69±0.10	0.15±0.11	-0.82±0.10	-0.35±0.14
Mg I	1343	-1.33±0.11	-1.40±0.08	-1.75±0.04	-1.20±0.09	-1.86±0.08	-1.94±0.07	-2.04±0.12	-2.07±0.09	-1.58±0.05	-1.29±0.06	-2.14±0.05	-2.18±0.12
Al I	1652	-1.97±0.16	-	-	-1.45±0.13	-	-	-	-2.21±0.16	-	-	-3.17±0.10	-2.06±0.15
Si I	1314	-	-	-1.62±0.10	-1.29±0.03	-	-1.79±0.12	-	-	-	-0.84±0.10	-1.88±0.10	-
S I	672	-0.31±0.07	-0.42±0.13	-0.60±0.08	-0.66±0.03	-0.21±0.15	-0.58±0.04	0.31±0.10	-0.23±0.07	-0.23±0.07	0.23±0.10	-0.54±0.02	-0.14±0.06
K I	993	-0.99±0.15	-	-1.24±0.12	-1.03±0.08	-0.86±0.15	-1.65±0.14	-	-1.1±0.15	-1.55±0.10	-	-	-0.44±0.15
Ca I	1535	-1.55±0.12	-1.87±0.05	-1.75±0.05	-1.39±0.07	-2.30±0.08	-1.92±0.11	-1.68±0.14	-2.05±0.11	-1.79±0.03	-1.36±0.07	-2.34±0.10	-1.67±0.13
Ca II	1535	-2.10±0.14	-	-	-1.65±0.13	-2.75±0.16	-	-2.29±0.12	-2.38±0.15	-	-	-	-
Fe I	1338	-1.70±0.11	-1.74±0.06	-1.76±0.05	-1.32±0.06	-2.04±0.10	-1.81±0.10	-1.81±0.12	-2.19±0.15	-1.79±0.03	-1.01±0.07	-2.37±0.03	-2.14±0.11
Fe II	1338	-1.88±0.07	-1.91±0.03	-1.94±0.07	-1.49±0.07	-2.20±0.14	-2.01±0.08	-1.98±0.08	-2.46±0.11	-1.89±0.04	-1.06±0.07	-2.49±0.02	-2.44±0.09

**Notes:** The condensation temperatures for C and N were adopted from [Lodders \(2003\)](#), the condensation temperatures for all other elements were adopted from [Wood et al. \(2019\)](#). Uncertainties below 0.1 dex are expected for elemental abundances derived from a small (2-4) number of lines displaying individual abundances, which are similar and stable within the uncertainty range of atmospheric parameters.

**Table E2.** Atmospheric parameters and differential NLTE corrections for studied elemental abundances of transition disc targets.

Name	CT Ori (#1)	ST Pup (#2)	RU Cen (#3)	AC Her (#4)	AD Aql (#5)	EP Lyr (#6)	DY Ori (#7)	AF CrI (#8)	GZ Nor (#9)	V1504 Sco (#10)	LMC V0770 (#11)	LMC V3156 (#12)
$T_{\text{eff}}$	5940±120	5340±80	6120±80	6140±100	6200±170	6270±160	6160±70	6110±110	4830±20	5980±90	5750±100	6160±130
$\log g$	1.01±0.18	0.20±0.10	1.46±0.15	1.27±0.16	1.67±0.45	1.24±0.18	0.88±0.14	0.96±0.21	0.00±0.18	0.98±0.17	0.00±0.18	1.38±0.20
[Fe/H]	-1.89±0.11	-1.92±0.08	-1.93±0.08	-1.47±0.08	-2.20±0.09	-2.03±0.17	-2.03±0.04	-2.47±0.05	-1.89±0.11	-1.05±0.07	-2.61±0.05	-2.48±0.04
C I	-0.13	-0.11	-0.13	-0.10	-0.14	-0.13	-0.23	-0.14	-0.23	-0.15	-0.12	-0.18
N I	-0.11	–	-0.14	-0.13	-0.14	-0.19	-0.30	-0.26	-0.14	-0.20	–	–
O I	-0.05	0.00	0.00	0.00	0.00	0.01	-0.09	0.00	-0.53	0.00	-0.14	0.00
Na I	-0.16	-0.12	-0.11	-0.15	-0.15	-0.38	-0.25	-0.77	-0.18	-0.33	-0.12	-0.82
Mg I	0.03	0.05	-0.07	0.00	0.02	-0.03	-0.05	-0.04	0.07	-0.08	0.01	0.03
Al I	0.43	–	–	0.41	–	–	–	0.60	–	–	0.66	0.58
Si I	–	–	-0.14	-0.11	–	-0.13	–	–	–	-0.09	0.11	–
S I	-0.14	-0.08	-0.18	-0.17	-0.24	-0.20	-0.31	-0.16	-0.11	-0.18	-0.18	-0.21
K I	-0.52	–	-0.50	-0.48	-0.77	-0.24	–	-0.29	-0.24	–	–	-0.78
Ca I	0.09	0.17	0.11	0.06	0.13	0.10	0.08	0.17	0.13	0.05	0.22	0.12
Ca II	-0.29	–	–	-0.08	-0.11	–	-0.25	-0.15	–	–	–	–
Fe I	0.15	0.17	0.17	0.15	0.20	0.17	0.16	0.27	0.11	0.05	0.24	0.33
Fe II	0.01	0.01	0.01	-0.01	0.01	0.01	0.00	0.03	0.00	-0.03	0.01	0.04



**APPENDIX F: INDIVIDUAL CORRELATION PLOTS**

In Fig. F1, we show the strong correlations and anti-correlations (with Spearman's coefficient  $|\rho| \geq 0.6$ ) between different parameters of the studied sample (see Section 6.1). We note that AF Crt (#8) and V1504 Sco (#10) were excluded from luminosity plots, since the luminosities of these edge-on targets are less reliable.

This paper has been typeset from a  $\text{\TeX}/\text{\LaTeX}$  file prepared by the author.

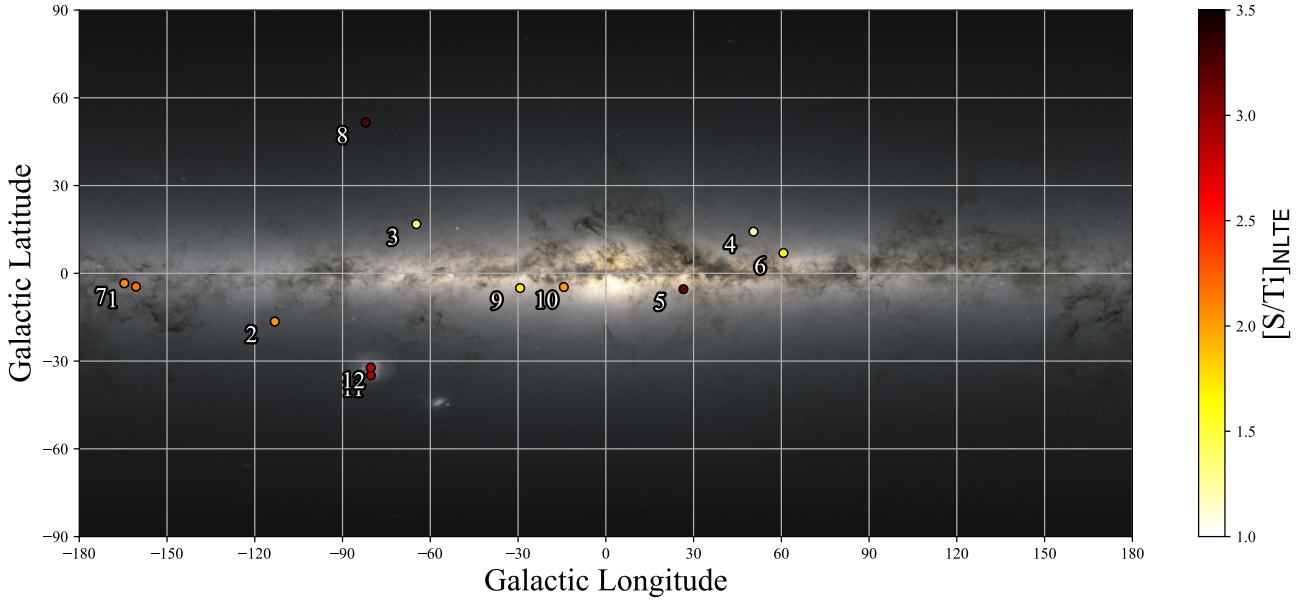


**Figure E1.** Spatial distribution of the transition disc targets. The targets are labelled by their IDs and coloured by the  $[S/Ti]_{NLTE}$  values derived in this study (see Table 5).

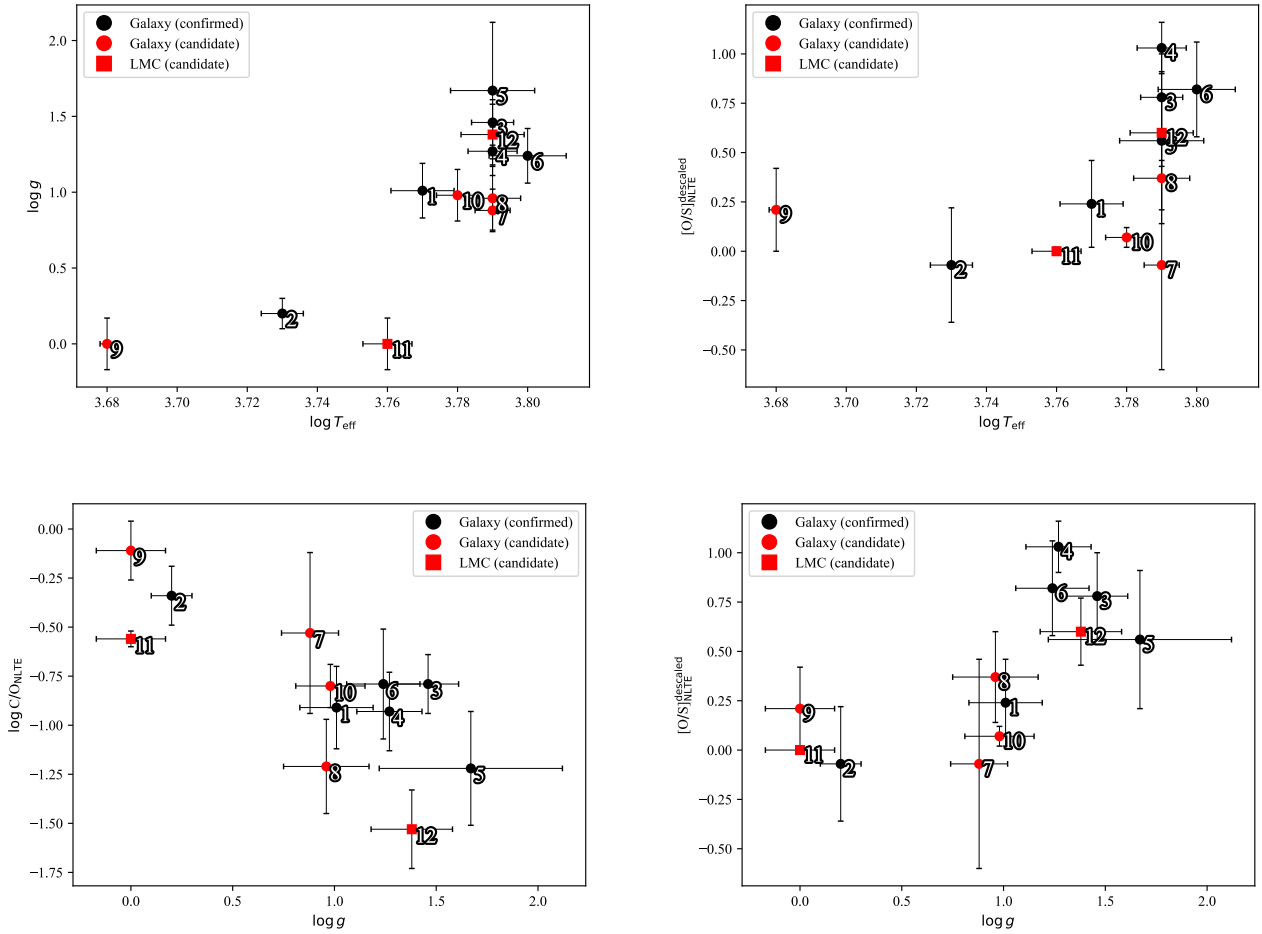


**Figure F1.** The strongest individual correlations in transition disc targets (see Section 6.1). The legend for the symbols and colours used is included within the plot. The targets are marked with their IDs.

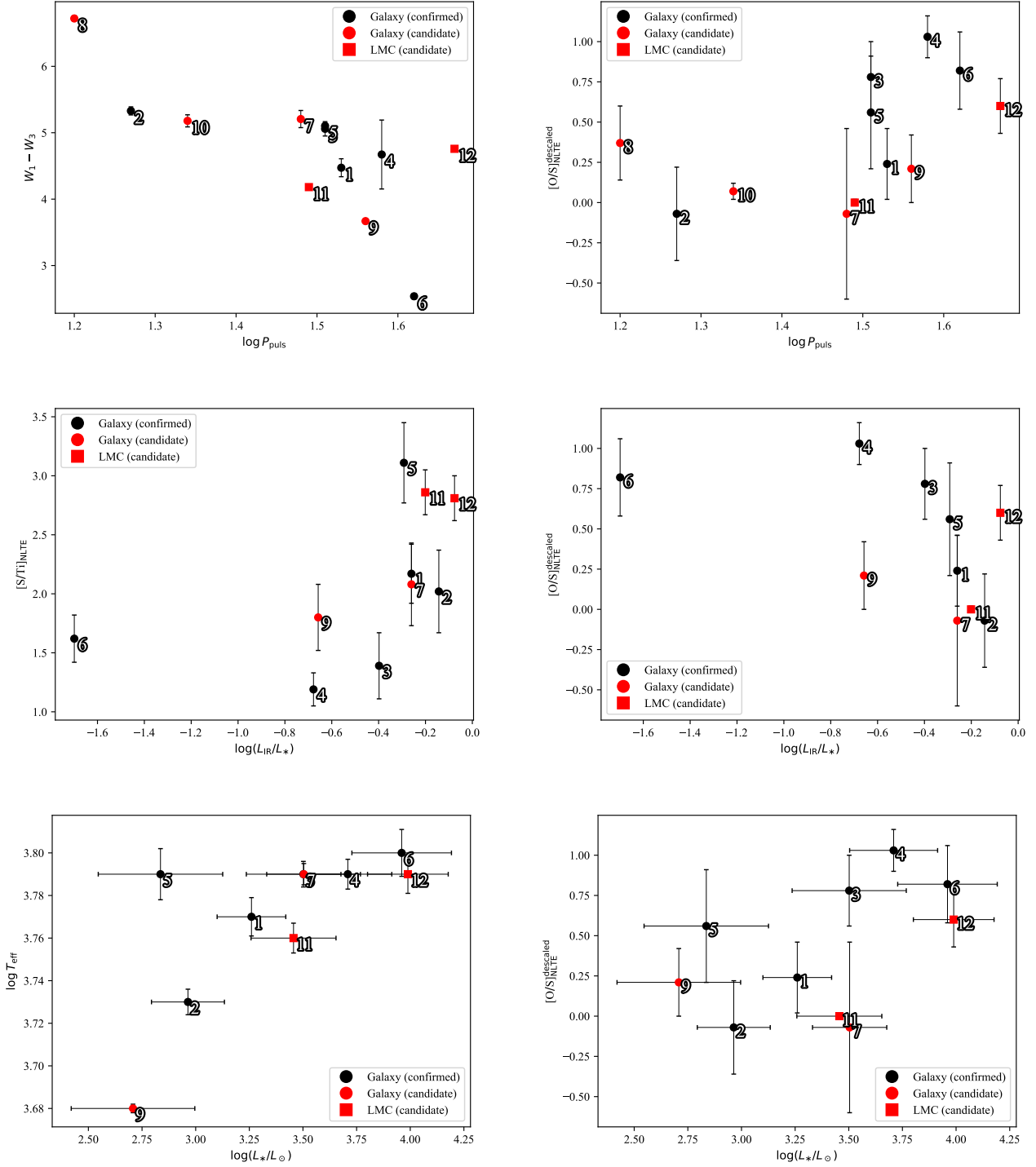


**Figure F2.** The strongest individual correlations in transition disc targets (see Section 6.1). The legend for the symbols and colours used is included within the plot. The targets are marked with their IDs.